PERGAMON

International Journal of Multiphase Flow 26 (2000) 1675–1706

International Journal of Multiphase Flow

www.elsevier.com/locate/ijmulflow

An all-pressure fluid drop model applied to a binary mixture: heptane in nitrogen

K. Harstad, J. Bellan*

Jet Propulsion Laboratory, California Institute of Technology, Pasadena, CA 91109, USA

Received 19 May 1999; received in revised form 20 October 1999

Abstract

The differences between subcritical liquid drop and supercritical fluid drop behavior are shown to be a direct consequence of the length scales near the fluid drop boundary. Under subcritical, evaporative high emission rate conditions, a film layer is present in the inner part of the drop surface which contributes to the unique determination of the boundary conditions; it is this film layer in conjunction with evaporation which gives to the solution its convective–diffusive character. In contrast, under supercritical conditions the boundary conditions contain a degree of arbitrariness due to the absence of a physical surface, and the solution has then a purely diffusive character. Results from simulations of a free fluid drop under no-gravity conditions are compared to microgravity experimental data from suspended, large drop experiments at high, low and intermediary temperatures and in a range of pressures encompassing the sub- and supercritical regime. Despite the difference between the conditions of the simulations and the experiments, the time rate of variation of the drop diameter square is remarkably well predicted in the linear curve regime. Consistent with the optical measurements, in the simulations the drop diameter is determined from the location of the maximum density gradient. Detailed time-wise comparisons between simulations and data show that this location is very well predicted at 0.1 MPa. As the pressure increases, the data and simulations agreement becomes good to fair, and the possible reasons for this discrepancy are discussed. Simulations are further conducted for a small drop, such as that encountered in practical applications, over a wide range of specified, constant far field pressures. Additionally, a transient pressure simulation crossing the critical point is also conducted. Results from these simulations are analyzed and major differences between the sub- and supercritical behavior are explained. In particular, it is shown that the classical calculation of the Lewis number gives erroneous results at supercritical conditions, and that an effective Lewis number previously

* Corresponding author.
E-mail address: josette.bellan@jpl.nasa.gov (J. Bellan).

0301-9322/00/$ - see front matter
PII: S0301-9322(99)00108-1

defined gives correct estimates of the length scales for heat and mass transfer at all pressures. © 2000 Published by Elsevier Science Ltd.

Keywords: Supercritical/subcritical fluid drops

1. Introduction

The behavior of fluids under a wide range of pressures is of both fundamental and great practical interest. Oil in underground reservoirs is naturally stored at very high pressures, and as it is extracted it eventually reaches the atmospheric pressure. Two examples of practical situations in which fluids experience large changes in pressures in a very short time are Diesel engines and aircraft engine combustion chambers. In both cases the energy that powers the engine is produced by the burning of atomized hydrocarbons with air; the word 'atomized' is used here in a very general sense to mean the disintegration of a fluid without reference to any particular configuration or mechanism. According to well-established thermodynamic theory (Hirshfelder et al., 1964; Prausnitz et al., 1986; American Petroleum Institute, 1992), once either the reduced pressure ($p_r = p/p_c$) or the reduced temperature ($T_r = T/T_c$) is larger than unity (the subscript 'c' denotes 'critical'), in the (p, V, T) system of coordinates there is no longer the possibility of a two-phase region, and instead there is only a single-phase region (Hirshfelder et al., 1964). Here p, T and V are the temperature, pressure and volume, respectively, and the subscript 'r' denotes 'reduced'. The general term for the substance is fluid (neither a gas nor a liquid) and it is in a supercritical state. Considering that the critical pressure of most fuel hydrocarbons used in these engines is in the range of 1.5–3 MPa, and the fact that the maximum pressure attained in the combustion chamber is about 6 MPa, it is clear that the fuel will experience both subcritical and supercritical conditions during the operation of the engine.

Despite the fact that supercritical fluids occur both in nature and in industrial situations, the fundamentals of their behavior is not well understood because supercritical fluids combine the characteristics of both liquids and gases, and therefore their behavior is not intuitive. There are several specific reasons for the lack of understanding: First, data from (mostly optical) measurements can be very misleading because regions of high density thus observed are frequently identified with liquids. A common misconception is that if in an experiment one can optically identify 'drops' and 'ligaments', the observed fluid must be in a liquid state. This inference is incorrect because in fact optical measurements detect any large change (i.e. gradients) in density. Thus, the density ratio may be well below $O(10^3)$ that characterizes its liquid/gas value, but the measurement will still identify a change in the index of refraction providing that the change is sudden (steep gradients). As shown by simulations of supercritical fluids of Harstad and Bellan (1998) under certain conditions the density gradients may remain large during the supercritical binary fluids mixing, thus making them optically identifiable. Therefore, there is no inconsistency between the optical observation of high density regions and the fluids being in a supercritical state. A second misconception is that because a fluid has a liquid-like density, it is appropriate to model it as a liquid. However, such fluids may have

liquid-like densities while their transport properties differ from those of a liquid. Table 1 shows the percent ratio of the thermal conductivity of fluid propane compared to that of the liquid at the same temperature. The calculations were performed using the plotted values of Reid et al. (1987) (Fig. 10-5). Since propane has a relatively large p_c (42.5 bar), the values of p_r are rather low compared to the corresponding ones for hexadecane (a neat fuel representative of Diesel fuel) at the same p because p_c of hexadecane is much lower (14.1 bar). Following the procedure for calculating conductivities at large p_r's knowing the conductivity at the same T_r but at a lower p_r (American Petroleum Institute, 1992, procedure 12A4.1), one finds that the discrepancy increases with increasing p_r and T_r, that is with increased pressure and fluid heating. Therefore, although a fluid under supercritical conditions may have a liquid-like density, it is not appropriate to model it as a liquid not only because the equation of state will be incorrect (and thus the density change in response to the fluid heating will be different from that of the liquid), but also because a fluid heats up differently from a liquid. In fact, it is not only the thermal conductivity which has a different value, but most important, the transport matrix of a general fluid has additional terms coupling the species and energy equations through temperature and molar fraction gradients, respectively. Harstad and Bellan (1999) have shown that as a result of these additional terms, under supercritical conditions the effective length scales for heat and mass diffusion increase and decrease, respectively, in comparison with those at subcritical conditions. This indicates that the mathematical solution of the system of equations might have different characteristics in the subcritical and supercritical regimes.

Studies of drop behavior over a wide range of pressures were performed in the past (Yang et al., 1994; Delplanque and Sirignano, 1993; Haldenwang et al., 1996, and the review of Givler and Abraham, 1996), however, none of these studies identified the crucial differences between the subcritical and supercritical behavior. In fact, in two of these studies (Yang et al., 1994; Haldenwang et al., 1996), it was found that the subcritical and supercritical behavior is similar as the drop diameter decreased according to the classical d^2-law (Williams, 1965) over a wide range of pressures and drop diameters, d.

The present study is devoted to the exploration of differences in fluid-behavior characteristics under subcritical and supercritical conditions in the particular case of fluid drops; the fluid drop case was selected because of the availability of experimental observations for model validation. We show in particular that the d^2-law is obeyed only in the subcritical regime. Section 2 presents a brief summary of our model (Harstad and Bellan, 1998) based upon fluctuation–dissipation theory; more details of our model can be found in Harstad and Bellan

Table 1
Percent error in the calculation of thermal conductivity of propane if calculated as for a liquid instead of a fluid

$p_r(p)$	$T_r(T)$		
	0.81 (300 K)	0.86 (320 K)	0.92 (340 K)
2.35 (100 bar)	10%	13.5%	13.5%
7.06 (300 bar)	25%	32%	35%

(1998, 1999). In Section 3, we expand our previous supercritical calculation (Harstad and Bellan, 1998) of the fluid drop radius to include the subcritical regime; in particular, we show that there is a major difference between the subcritical and supercritical behavior which is intimately related to the length scales near the fluid drop boundary. Results from simulations are compared in Section 4 to data for heptane drops in nitrogen at high, intermediate and low temperatures and in the 0.1–5 MPa pressure range, and the theory is validated. The comparison with high temperature experimental data allows us to first determine the value of the assumed constant thermal diffusion factor; once this is done, the value is confirmed at intermediate temperatures by comparing with the data, and further model validations are conducted with this value at low temperatures. We further present numerical predictions for small drop sizes in high temperature surroundings (which are of practical interest in the combustion chambers of propulsion systems and for which detailed data for validation do not exist) at both constant and varying pressure crossing the critical point of the fluid, and offer comments regarding the difficulties of performing calculations crossing the critical point. Finally, Section 5 is devoted to conclusions.

2. Model equations

The configuration studied is that of a single spherical drop in a medium with specified far field conditions. These far field values are identified by the subscript 'e' and the location of the far field boundary, $R_e(t)$, where R is a specified radial location, is calculated in a Lagrangian way to be that of null mass flux.

The conservation equations are based upon Keizer's (Keizer, 1987) fluctuation–dissipation theory which has the distinct advantage of formally accounting for non-equilibrium processes. This formalism therefore leads to the most general fluid equations where the partial molar fluxes, $\vec{J}_i$, for species i, and the heat flux, $\vec{q}$, are related to thermodynamic quantities as follows:

$$\vec{J}_i = L_{iq}\nabla\beta - \sum_j^N L_{ij}\nabla\left(\beta\mu_j\right), \qquad \vec{q} = L_{qq}\nabla\beta - \sum_j^N L_{qj}\nabla\left(\beta\mu_j\right) \tag{1}$$

where $\beta \equiv 1/(R_u T)$ and N is the total number of species; the expression in Eq. (1) is called the Irwing–Kirkwood (IK) form (Sarman and Evans, 1992) of the heat flux. Here R_u is the universal gas constant, μ_j is the chemical potential of species j, L_{ij} are the Fick's diffusion elements, L_{qq} is the Fourier thermal diffusion element, L_{iq} are the Soret diffusion, L_{qj} are the Dufour diffusion elements, and the Onsager relations state that $L_{ij} = L_{ji}$ and $L_{iq} = L_{qi}$. Additionally, conservation of fluxes and mass in the system imply that $\sum_i^N m_i\vec{J}_i = \vec{0}$ and $\sum_i^N L_{ij}m_i = 0$ for $j \in [1, N]$ and $j = q$, where m_i is the molar mass of species i.

Using the thermodynamic relationship

$$\mathrm{d}\left(\beta\mu_j\right) = \beta\left(v_j\,\mathrm{d}p - h_j\,\mathrm{dln}\,T\right) + \left(\sum_1^{N-1}\alpha_{D_{ji}}\,\mathrm{d}X_i\right)/X_j \tag{2}$$

where

$$h_j = \frac{\partial h}{\partial X_j} = \mu_j - T\frac{\partial \mu_j}{\partial T} \tag{3}$$

$$v_j = \frac{\partial v}{\partial X_j} = \partial \frac{\mu_j}{\partial p} \tag{4}$$

$$\alpha_{\mathrm{D}_{ij}} \equiv \beta X_i \frac{\partial \mu_i}{\partial X_j} = \frac{\partial X_i}{\partial X_j} + X_i \frac{\partial \ln \gamma_i}{\partial X_j} \tag{5}$$

one can calculate $\vec{J}_i$ and $\vec{q}$ from Eqs. (1) and (2), providing that the elements, L_{ij}, can be calculated. Here v_j, h_j, X_j, and γ_i are the partial molar volume, enthalpy, molar fraction and activity coefficient, respectively, while v and h are the total molar volume and enthalpy, respectively. The coefficients $\alpha_{\mathrm{D}_{ij}}$ are called mass diffusion factors, and $\gamma_i \equiv \varphi_i/\varphi_i^o$ where φ is the fugacity coefficient and the superscript 'o' denotes the pure ($X_i = 1$) limit.

The transport matrix has the advantage of allowing a natural definition of the transport coefficients therefore relating its elements to measurable/calculable quantities. Thus, a thermal conductivity is defined by $\lambda_{\mathrm{IK}} \equiv \beta L_{qq}/T$ (subscript 'IK' designates quantities related to this form of the heat flux). However, λ_{IK} does not correspond to the kinetic theory (subscript KT) thermal conductivity because, in particular, it is not the only coefficient of ∇T in $\vec{q}$; the significance of this observation is discussed below. Also related to the transport matrix, two transport coefficient matrices may be defined: a symmetric diffusion coefficient matrix, $D_{m,ij}$, and an antisymmetric thermal diffusion factor matrix, $\alpha_{\mathrm{IK},ij}$, through

$$L_{ij} \equiv -D_{m,ij} n Y_i Y_j, \quad i \neq j \tag{6}$$

$$\beta L_{iq} \equiv X_i \sum_{j \neq i} \alpha_{\mathrm{IK},ij} n Y_j D_{m,ij} \tag{7}$$

with the consequence that

$$L_{ii} = X_i \sum_{j \neq i} \left(\frac{m_j}{m}\right) n Y_j D_{m,ij}. \tag{8}$$

Here n and Y_j are the molar density and species mass fraction, while m is the average molar mass of the mixture. Thus, the knowledge of λ_{IK} and the $D_{m,ij}$ and $\alpha_{\mathrm{IK},ij}$ matrices allows the calculation of the transport matrix.

In terms of these new matrices, the general form of the molar fluxes for $i \in [1, N]$ is

$$\vec{J}_i = -n\left[X_i\left(D_{T,i}\nabla \ln T + D_{p,i}\nabla \ln p\right) + \sum_{k=1}^{N-1} \mathscr{D}_{ik} \nabla X_k\right] \tag{9}$$

where

$$D_{T,i} \equiv \sum_j Y_j \left[\alpha_{\mathrm{IK},ij} - \beta \left(\frac{m_i m_j}{m} \right) \left(\frac{h_i}{m_i} - \frac{h_j}{m_j} \right) \right] D_{m,ij} \tag{10}$$

$$D_{p,i} \equiv \beta p \sum_j Y_j \left(\frac{m_i m_j}{m} \right) \left(\frac{v_i}{m_i} - \frac{v_j}{m_j} \right) D_{m,ij} \tag{11}$$

$$\mathscr{D}_{ik} \equiv \sum_j D_{m,ij} \left(\frac{m_j}{m} \right) \left(Y_j \alpha_{\mathrm{D}_{ik}} - Y_i \alpha_{\mathrm{D}_{jk}} \right) \tag{12}$$

and the form of the heat flux is

$$\vec{q} = -\lambda'_{\mathrm{IK}} \nabla T - n R_{\mathrm{u}} T \left(D_{qp} \nabla \ln p + \sum_k \mathscr{D}_{qk} \nabla X_k \right) \tag{13}$$

where λ'_{IK} is another form of the IK thermal conductivity

$$\lambda'_{\mathrm{IK}} = \lambda_{\mathrm{IK}} - \left(\frac{\rho}{T} \right) \sum_{i>j} Y_i Y_j \left(\frac{h_i}{m_i} - \frac{h_j}{m_j} \right) \alpha_{\mathrm{IK},ij} D_{m,ij} \tag{14}$$

$$D_{qp} \equiv \beta m p \sum_{i>j} Y_i Y_j \left(\frac{v_i}{m_i} - \frac{v_j}{m_j} \right) \alpha_{\mathrm{IK},ij} D_{m,ij} \tag{15}$$

$$\mathscr{D}_{qk} \equiv \sum_{i>j} \left(Y_j \alpha_{\mathrm{D}_{ik}} - Y_i \alpha_{\mathrm{D}_{jk}} \right) \alpha_{\mathrm{IK},ij} D_{m,ij}. \tag{16}$$

Note that unlike λ_{IK}, λ'_{IK} is the only coefficient of ∇T in the heat flux $\vec{q}$.

2.1. Conservation equations for a multicomponent mixture

In spherical geometry the conservation equations are:

- continuity:

$$\frac{\partial \rho}{\partial t} + \frac{1}{r^2} \frac{\partial \left(r^2 \rho u \right)}{\partial r} = 0 \tag{17}$$

  where ρ is the mass density, u is the radial velocity, t is the time and r is the radial coordinate.
- momentum conservation:

$$\frac{\partial (\rho u)}{\partial t} + \frac{1}{r^2} \frac{\partial \left(r^2 \rho u u \right)}{\partial r} + \frac{\partial p}{\partial r} = \frac{\partial \tau_{rr}}{\partial r} + \frac{3 \tau_{rr}}{r} \tag{18}$$

  where $\tau_{rr} = (4/3)\eta(\partial u/\partial r - u/r)$ is the stress tensor and η is the mixture viscosity.

- species conservation:

$$\rho\frac{\mathrm{D}Y_i}{\mathrm{D}t} = -m_i\nabla\cdot\vec{J}_i \tag{19}$$

where $\mathrm{D}/\mathrm{D}t \equiv \partial/\partial t + u(\partial/\partial r)$.

- energy equation:

$$nC_\mathrm{p}\frac{\mathrm{D}T}{\mathrm{D}t} = \alpha_\mathrm{v}T\frac{\mathrm{D}p}{\mathrm{D}t} - \nabla\cdot\vec{q} + \Phi_\mathrm{v} + \sum_j^N h_j\nabla\cdot\vec{J}_j \tag{20}$$

where C_p is the mixture molar heat capacity at constant pressure, $\alpha_\mathrm{v} = [(\partial v/\partial T)_{p,X_i}]/v$ is the thermal expansion ratio, and $\Phi_\mathrm{v} = (4/3)\eta(\partial u/\partial r - u/r)^2$ is the viscous dissipation.

2.2. Relationship between kinetic theory and measured values of λ and $\alpha_{\mathrm{IK},\,ij}$ for multicomponent mixtures

As mentioned above, λ_IK in Eq. (1) might not be the quantity measured in experiments determining thermal conductivities because it is not the coefficient of the temperature gradient in the heat flux expression; this expression has Soret term contributions from the molar flux (the cross terms) that also contain temperature gradients. Another form of the heat flux is given by the Bearman–Kirkwood (BK) expression (Sarman and Evans, 1992)

$$\vec{q}'' \equiv \vec{q} - \sum_j h_j\vec{J}_j = L''_{qq}\nabla\beta - \sum_j^N L''_{qj}\nabla(\beta\mu_j) = \tilde{L}_{qq}\nabla\beta - \sum_j^N L''_{qj}\left[\nabla(\beta\mu_j) - h_j\nabla\beta\right] \tag{21}$$

where according to Eq. (2)

$$\nabla(\beta\mu_j) - h_j\nabla\beta = \beta v_j\nabla p + \left(\sum_i \alpha_{\mathrm{D}_{ji}}\nabla X_i\right)/X_j. \tag{22}$$

If one defines a BK thermal conductivity by $\lambda_\mathrm{BK} \equiv \beta\tilde{L}_{qq}/T$, this is now the only coefficient of the temperature gradient in the BK form of the heat flux, Eq. (21). In the same manner as $\alpha_{\mathrm{IK},ij}$, one may define BK thermal diffusion factors $\alpha_{\mathrm{BK},ij}$ by

$$\beta L''_{iq} \equiv X_i\sum_{j\neq i}\alpha_{\mathrm{BK},ij}nY_jD_{m,ij}. \tag{23}$$

Tedious but straightforward calculations show that for a multicomponent system

$$\lambda_\mathrm{BK} = \lambda'_\mathrm{IK} - \left(\frac{\rho}{T}\right)\sum_{i>j}\left(\frac{h_i}{m_i} - \frac{h_j}{m_j}\right)Y_iY_j\alpha_{\mathrm{BK},ij}D_{m,ij}. \tag{24}$$

but neither λ_BK nor λ'_IK coincide with the kinetic theory thermal conductivity in the low pressure limit, and therefore cannot be considered to be an appropriate definition of the

thermal conductivity. However, if one defines a thermal conductivity, λ, through the relationship

$$\lambda \equiv \lambda'_{\mathrm{IK}} - R_{\mathrm{u}} n \sum_{i>j} X_i X_j \alpha_{\mathrm{BK},ij} \alpha_{\mathrm{IK},ij} D_{m,ij}, \tag{25}$$

then λ has the distinctive property that in the low pressure limit it consistently becomes λ_{KT} (i.e. $\lim_{p\to 0}\lambda = \lambda_{\mathrm{KT}}$; see Chapman and Cowling, 1970); it also has the property that non-negative entropy production requires $\lambda \geq 0$. Moreover, it can be shown that

$$\alpha_{\mathrm{BK},ij} = \alpha_{\mathrm{IK},ij} - \alpha_{h,ij} \tag{26}$$

where

$$\alpha_{h,ij} \equiv \left(\frac{m_i m_j}{m}\right)\left(\frac{h_i}{m_i} - \frac{h_j}{m_j}\right)/(R_{\mathrm{u}} T), \tag{27}$$

and that $\lim_{p\to 0}(\alpha_{\mathrm{BK},ij}) = \alpha_{\mathrm{KT},ij}$. Note that crossterms vary in $\vec{q}$ as $\alpha_{\mathrm{IK},ij}$, and those in $\vec{J}_i$ and $\vec{q}''$ vary as $\alpha_{\mathrm{BK},ij}$.

For a pure substance, $\lambda_{\mathrm{BK}} = \lambda_{\mathrm{IK}} = \lambda'_{\mathrm{IK}} = \lambda\ (= \lambda_{\mathrm{KT}})$; however, this is no longer the case for mixtures. Therefore, particular care is taken in the present simulations to insure that the available data for individual substances is used to calculate λ according to the well established mixing rules of Teja and Rice explained in Reid et al. (1987).

Thermal diffusion factors have been calculated by Vogelsang and Hoheisel (1988) and Sarman and Evans (1992) using Molecular Dynamics theory; these calculations are very computationally-intensive. Thermal diffusion ratios for ternary mixtures are rarely reported, an exception being Singh et al. (1983) for a Ne–Ar–Kr gaseous mixture. Measurements of thermal diffusion factors have been made either in thermodiffusion cells (Bert and Dupuy-Philon, 1997; Li et al., 1994) or in thermogravitational columns (Bou-Ali et al., 1998; Ecenarro et al., 1990, 1993). Each of these systems presents some difficulties for performing the measurements. For example, thermal diffusion cells measurements may be affected by convective effects or by the long time needed to achieve uniformity in the two cells, whereas thermogravitational measurements are affected by parasitic convective effects and nonuniformities in the wall temperature. Generally, measured values of either $\alpha_{\mathrm{BK},ij}$ or $\alpha_{\mathrm{IK},ij}$ are very scarce (see tabulated values in Bird et al., 1960; Chapman and Cowling, 1970), and although some data exists near the critical point (Ecenarro et al., 1993), we are not aware of extensive comprehensive data at supercritical conditions. Therefore, the value of $\alpha_{\mathrm{BK},ij}$ or $\alpha_{\mathrm{IK},ij}$ must be determined from comparisons with experimental data (see below).

For a binary mixture $D_{m,12}$ is the binary diffusion coefficient D_m and

$$\vec{q} = -(\alpha_{\mathrm{IK}} R_{\mathrm{u}} T)\vec{J}_{\mathrm{b}} - \lambda'_{\mathrm{IK}} \nabla T \tag{28}$$

$$\vec{q}'' = -(\alpha_{\mathrm{BK}} R_{\mathrm{u}} T)\vec{J}_{\mathrm{b}} - \lambda_{\mathrm{BK}} \nabla T \tag{29}$$

$$\vec{J}_1 = -(m_2/m)\left(\vec{J}_{\mathrm{b}} + X_1 X_2 \alpha_{\mathrm{BK}} n \mathrm{D}_m \nabla \ln T\right) \tag{30}$$

$$\vec{J}_{\mathrm{b}} = nD_m\left[\alpha_D \nabla X_1 + \beta(m_1 m_2 X_1 X_2/m)(v_1/m_1 - v_2/m_2)\nabla p\right] \tag{31}$$

$$\lambda_{\mathrm{BK}} = \lambda + X_1 X_2 (\alpha_{\mathrm{BK}})^2 R_{\mathrm{u}} n D_m \tag{32}$$

$$\lambda'_{\mathrm{IK}} = \lambda + X_1 X_2 \alpha_{\mathrm{IK}} \alpha_{\mathrm{BK}} R_{\mathrm{u}} n D_m \tag{33}$$

$$\alpha_{\mathrm{BK}} = \alpha_{\mathrm{IK}} - \alpha_h \tag{34}$$

and since α_h may be either positive or negative and have a relatively large magnitude (e.g. the LO_x–H_2 system in Harstad and Bellan, 1998), α_{BK} and α_{IK} may have very different values.

These considerations show that it is essential to understand the intricacies of the transport matrix in order to enable quantitative calculations that can be validated by experimental observations. Some of the results presented below investigate these intricacies even further by exploring the determination of α_{BK} and α_{IK} from existing measurements over a wide range of (p, T) in conjunction with model validation.

3. Boundary conditions for a binary mixture

The detailed boundary conditions at $r = R_{\mathrm{d}}$, where R_{d} is the drop radius, have been derived in Harstad and Bellan (1998) and are summarized here only. The subscripts 'b' and 'd' indicate the drop boundary and drop related quantities, respectively, and the superscripts 'L' and 'G' refer to the initial heptane and nitrogen side of the drop boundary, respectively.

- mass balance:

$$\rho_{\mathrm{b}}^{\mathrm{G}}\left(u_{\mathrm{b}}^{\mathrm{G}} - \frac{\mathrm{d}R_{\mathrm{d}}}{\mathrm{d}t}\right) = \rho_{\mathrm{b}}^{\mathrm{L}}\left(u_{\mathrm{b}}^{\mathrm{L}} - \frac{\mathrm{d}R_{\mathrm{d}}}{\mathrm{d}t}\right) \tag{35}$$

- relationship between R_{d} and the emission flux F_{ems}. By definition of the mass emission flux, $F_{\mathrm{ems}} \equiv -(1/A_{\mathrm{d}})\mathrm{d}M/\mathrm{d}t$, where M is the drop mass and A_{d} is the drop boundary area, which is consistent with

$$F_{\mathrm{ems}} = \rho_{\mathrm{b}}^{\mathrm{L}}\left(u_{\mathrm{b}}^{\mathrm{L}} - \mathrm{d}R_{\mathrm{d}}/\mathrm{d}t\right). \tag{36}$$

- heat balance:

$$q_{\mathrm{r,\,b}}^{\mathrm{G}} - q_{\mathrm{r,\,b}}^{\mathrm{L}} = -\left[\frac{h_2^{\mathrm{G}} + \left(h_1^{\mathrm{G}} - h_2^{\mathrm{G}}\right)X_{1\mathrm{b}}^{\mathrm{G}}}{m^{\mathrm{G}}} - \frac{h_2^{\mathrm{L}} + \left(h_1^{\mathrm{L}} - h_2^{\mathrm{L}}\right)X_{1\mathrm{b}}^{\mathrm{L}}}{m^{\mathrm{L}}}\right]F_{\mathrm{ems}} \tag{37}$$

  where $h_j^{\mathrm{G}} = h_j(p_{\mathrm{b}}, T_{\mathrm{b}}, X_{1\mathrm{b}}^{\mathrm{G}})$, $h_j^{\mathrm{L}} = h_j(p_{\mathrm{b}}, T_{\mathrm{b}}, X_{1\mathrm{b}}^{\mathrm{L}})$ and $h_1^{\mathrm{G}} - h_1^{\mathrm{L}}$ is the molar heat of evaporation whereas $h_2^{\mathrm{G}} - h_2^{\mathrm{L}}$ is the heat of solution. The subscript 'r' stands for radial component.
- balance of species 1 (chosen to be heptane) flux:

$$m_1\left(J_{1\mathrm{r,b}}^{\mathrm{G}} - J_{1\mathrm{r,b}}^{\mathrm{L}}\right) = \left(Y_{1\mathrm{b}}^{\mathrm{L}} - Y_{1\mathrm{b}}^{\mathrm{G}}\right)F_{\mathrm{ems}} \tag{38}$$

- non-equilibrium evaporation law. This is obtained by calculating the fluxes at the molecular level to yield

$$F_{\text{ems}} = \sum_{j=1,\,2}\left[\alpha_{\text{a}j} m_j u_{Tj}\left(n^{\text{G}}_{j,\text{equil}} - n^{\text{G}}_{j}\right)\right] \tag{39}$$

where $n^{\text{G}}_{j,\,\text{equil}}$'s are calculated from thermodynamic relationships (Prausnitz et al., 1986), u_{Tj} is the mean molecular velocity crossing a plane in one direction, and $\alpha_{\text{a}j}$ are accommodation coefficients. The expressions for $n^{\text{G}}_{j,\text{equil}}$'s are

$$n^{\text{G}}_{j,\text{equil}} = \frac{\rho^{\text{G}}_{\text{b}} X^{\text{L}}_{j\text{b}} \varphi^{\text{L}}_{j,\text{b}}}{\varphi^{\text{G}}_{j,\text{b}} m^{\text{G}}}. \tag{40}$$

Additional equations at $r = R_{\text{d}}$ are the momentum and the mixture equation of state which is used twice (once on each side of the boundary). Since u^{L}_{b} is calculated by integrating the continuity equation inside the drop, there is a total of eight equations and nine unknowns: u^{G}_{b}, $X^{\text{L}}_{1\text{b}}$, $X^{\text{G}}_{1\text{b}}$, $\rho^{\text{L}}_{\text{b}}$, $\rho^{\text{G}}_{\text{b}}$, R_{d}, T_{b}, p_{b} and F_{ems}; a ninth independent relationship exists only under subcritical conditions, as discussed below.

The indeterminacy of the boundary conditions for a fluid drop under supercritical conditions has already been discussed by Harstad and Bellan (1998). This is physically understandable since there is no true surface, and thus there is an arbitrariness as to the choice of the boundary to follow. At least three choices are reasonable: One may follow the pure fluid boundary as was done by Harstad and Bellan (1998). Another possibility is to follow the initial boundary separating the two fluids, this being the choice in the present calculation. The third possibility is to follow the point of maximum density gradient; although this is not the present choice, the point of maximum density gradient is calculated here à posteriori to indicate the location of the optically identified fluid drop. In contrast, under subcritical conditions the boundary to follow is the drop surface and the problem is fully determined.

There are other important consequences of the existence or lack of a surface at $r = R_{\text{d}}$. For example, under strong evaporative conditions a mass fraction 'film' layer exists inside the drop (Law and Law, 1982) and the thickness of this layer, $\delta_Y \ll \Delta r^-$ where Δr^- is the distance from the surface to the first grid point inside the drop. A detailed analysis (Harstad and Bellan, 1999) shows that an effective mass diffusivity D_{eff} can be defined as shown below, with the consequence that the film layer exists when $F_{\text{ems}} \gg \rho D_{\text{eff}}/\Delta r^-$. The value of D_{eff} and that of an equivalent λ_{eff} were calculated under the quasi-steady assumption in Harstad and Bellan (1999) by finding a set of two linear combinations of T and Y_1 for which Eqs. (19) and (20) can be approximately diagonalized. The radial fluxes are

$$\begin{aligned} -J_{1\text{r}} &= A_J \frac{\partial Y_1}{\partial r} + B_J \frac{\partial T}{\partial r} + C_J \frac{\partial p'}{\partial r} \\ -q_{\text{r}} &= A_q \frac{\partial T}{\partial r} + C_q \frac{\partial Y_1}{\partial r} + B_q \frac{\partial p'}{\partial r} \end{aligned} \tag{41}$$

where for a binary mixture the coefficients are

$$A_J = (m/m_1)nD_m\alpha_D \tag{42}$$

$$B_J = (m_2/m)nD_mX_1X_2(\alpha_{\mathrm{IK}} - \alpha_h)/T \tag{43}$$

$$C_J = (m_2/m)nD_m(m_1m_2X_1X_2/m)(v_1/m_1 - v_2/m_2)/(R_{\mathrm{u}}T) \tag{44}$$

$$A_q = \lambda + (\alpha_{\mathrm{IK}} - \alpha_h)\alpha_{\mathrm{IK}}R_{\mathrm{u}}nD_mX_1X_2 \tag{45}$$

$$C_q = \left[m^2/(m_1m_2)\right]nD_m\alpha_D\alpha_{\mathrm{IK}}R_{\mathrm{u}}T \tag{46}$$

$$B_q = nD_m\alpha_{\mathrm{IK}}(m_1m_2X_1X_2/m)(v_1/m_1 - v_2/m_2) \tag{47}$$

where according to the Gibbs–Duhem relationship $\alpha_D = \alpha_{D11} = \alpha_{D22} = -\alpha_{D12} = -\alpha_{D21}$ and

$$\alpha_h \equiv (m_1m_2/m)(h_1/m_1 - h_2/m_2)/(R_{\mathrm{u}}T). \tag{48}$$

Once the equations for T and Y_1 are diagonalized, the characteristic length scales for diffusional transport of the new set of variables are apparent, and this allows the definition of D_{eff} and λ_{eff}

$$\rho D_{\mathrm{eff}} = m_1A_J - \omega_T mC_q'/C_{\mathrm{p}} \tag{49}$$

$$\lambda_{\mathrm{eff}} = A_q' - \omega_Y(m_1/m)C_{\mathrm{p}}B_J \tag{50}$$

where

$$A_q' \equiv A_q - m_1\left(\frac{h_1}{m_1} - \frac{h_2}{m_2}\right)B_J \quad \text{and} \quad C_q' \equiv C_q - m_1\left(\frac{h_1}{m_1} - \frac{h_2}{m_2}\right)A_J \tag{51}$$

with

$$\omega_T = \sigma m_1C_{\mathrm{p}}B_J/m \quad \text{and} \quad \omega_Y = -\sigma C_q' \tag{52}$$

where σ is the positive root of the second-order algebraic equation

$$(m_1/m)C_{\mathrm{p}}B_JC_q'\sigma^2 + \left[A_q' - (m_1/m)C_{\mathrm{p}}A_J\right]\sigma - 1 = 0 \tag{53}$$

the other root being unphysical as it leads to singular behavior. These equations also allow the calculation of an effective Lewis number, $Le_{\mathrm{eff}} \equiv \lambda_{\mathrm{eff}}/(nC_{\mathrm{p}}D_{\mathrm{eff}})$ once the values of the dependent variables are known. The quasi-steady assumption does not remove the generality of the estimate since its essence is that of a characteristic length. One of the most important consequences of the mass fraction film layer existence is the direct relationship that exists between $Y_i(R_{\mathrm{d}} - \varepsilon)$ and $Y_i(R_{\mathrm{d}} + \varepsilon)$, where $\varepsilon \lll \max(\delta_Y, \delta_T)$; it is this relationship which provides the needed additional equation to fully determine the solution at the drop surface. This relationship can be formulated by considering the difference $\Delta Y_1^{\mathrm{L}} \equiv Y_1^{\mathrm{L}}(R_{\mathrm{d}} - \varepsilon) - Y_1^{\mathrm{L}}(R_{\mathrm{d}} - \Delta r^-)$

where $Y_1^{\mathrm{L}}(R_{\mathrm{d}}-\Delta r^-)$ represents the computational grid center value at the first adjacent position to the film layer inside the drop such that $\Delta r^- \gg \delta_Y$. Similarly, one may define $\Delta T^{\mathrm{L}} \equiv T^{\mathrm{L}}(R_{\mathrm{d}}-\varepsilon) - T^{\mathrm{L}}(R_{\mathrm{d}}-\Delta r^-)$. The variable $\xi_j \equiv \varphi_j^{\mathrm{L}}/\varphi_j^{\mathrm{G}}$ quantifies the Y_j jump across the drop surface and can be calculated from the state equation. For example, under strict equilibrium evaporation (i.e. $F_{\mathrm{ems}}=0$) conditions, $\xi_j=1$. For finite F_{ems} and for a binary mixture, its ratio to a reference state $F_{\mathrm{ref}}(\xi_1,\xi_2)$ can be defined by

$$F_{\mathrm{ems}} = \epsilon_F F_{\mathrm{ref}} \tag{54}$$

where

$$F_{\mathrm{ref}} \equiv \mathscr{B}_1(\xi_{\mathrm{av}}-\xi_1) + \mathscr{B}_2(\xi_2-\xi_{\mathrm{av}}) \tag{55}$$

$$\mathscr{B}_j \equiv \alpha_{\mathrm{a}j} m_j u_{Tj} n^{\mathrm{G}}, \quad j=1,2 \tag{56}$$

$$X_1^{\mathrm{L}}(R_{\mathrm{d}}-\varepsilon) = \frac{(\xi_2-1)}{(\xi_2-\xi_1)} - \epsilon_F \quad \text{and} \quad X_1^{\mathrm{G}}(R_{\mathrm{d}}+\varepsilon) = \frac{\xi_1(\xi_2-1)}{(\xi_2-\xi_1)} - \xi_{\mathrm{av}}\epsilon_F \tag{57}$$

$$X_2^{\mathrm{L}}(R_{\mathrm{d}}-\varepsilon) = \frac{(1-\xi_1)}{(\xi_2-\xi_1)} + \epsilon_F \quad \text{and} \quad X_2^{\mathrm{G}}(R_{\mathrm{d}}+\varepsilon) = \frac{\xi_2(1-\xi_1)}{(\xi_2-\xi_1)} + \xi_{\mathrm{av}}\epsilon_F \tag{58}$$

and consistently $F_{\mathrm{ref}}(1,1)=0$. A detailed analysis of the film layer yields then

$$\xi_{\mathrm{av}} = \frac{\mathscr{B}_2\xi_2 Y_1^{\mathrm{L}}(R_{\mathrm{d}}-\Delta r^-) + \mathscr{B}_1\xi_1 Y_2^{\mathrm{L}}(R_{\mathrm{d}}-\Delta r^-)}{\mathscr{B}_2 Y_1^{\mathrm{L}}(R_{\mathrm{d}}-\Delta r^-) + \mathscr{B}_1 Y_2^{\mathrm{L}}(R_{\mathrm{d}}-\Delta r^-)} \tag{59}$$

which provides the additional relationship between $X_1^{\mathrm{L}}(R_{\mathrm{d}}-\varepsilon)$ and $X_1^{\mathrm{G}}(R_{\mathrm{d}}+\varepsilon)$ and allows closure of the system of equations at the drop boundary.

Since under supercritical conditions the concept of latent heat, and therefore of evaporation, is not applicable [$(h_1^{\mathrm{G}}-h_1^{\mathrm{L}})\to 0$ as the critical point is approached], the above analysis does not hold. However, the film layer computational approach is still necessary if the grid Peclet number $Pe_{\mathrm{grid}} \geq O(1)$ in order to insure that all scales are resolved. Therefore, the formalism of the film layer is retained for computational purposes even under supercritical conditions, although the layer no longer exists physically. This is accomplished by a generalization of the layer equations so that the limit $F_{\mathrm{ems}}\to 0$ yields the form of the equations without the layer. Essentially, the solution in the supercritical regime has a diffusive character, whereas in the subcritical regime it has a diffusive–convective character where the convective part is introduced by the film layer and the evaporation.

At $R_{\mathrm{e}}(t)$ the dependent variables are specified.

4. Numerical method

The primitive variables are p, T, X_j (or Y_j) and u, however, the equations are analytically manipulated to facilitate calculations. For convenience, the density derivatives in Eq. (17) are

replaced using the relationship

$$\mathrm{d}\ln\rho = -\alpha_{\mathrm{v}}\,\mathrm{d}T + \kappa_T\,\mathrm{d}p + \sum_1^N \left(m_j/m - v_j/v\right)\mathrm{d}X_j \tag{60}$$

where $\kappa_T = -(1/v)(\partial v/\partial p)_{T,X_j}$ is the isothermal compressibility. Combining Eqs. (60), (17), (19) and (20) yields

$$\nabla\cdot\vec{u} = -\frac{\mathrm{D}\ln\rho}{\mathrm{D}t} = S_{\mathrm{u}} \tag{61}$$

where

$$S_{\mathrm{u}} = \alpha_{\mathrm{v}}\frac{\mathrm{D}T}{\mathrm{D}t} - \kappa_T\frac{\mathrm{D}p}{\mathrm{D}t} + \rho\sum_j \frac{v_j}{m_j}\frac{\mathrm{D}Y_j}{\mathrm{D}t} = \vec{k}_{\mathrm{u}}\cdot\vec{u} + \nu_{\mathrm{u}} \tag{62}$$

with

$$\vec{k}_{\mathrm{u}} = \alpha_{\mathrm{v}}\nabla T - \kappa_T\nabla p' + \rho\sum_j \frac{v_j}{m_j}\nabla Y_j \tag{63}$$

$$\nu_{\mathrm{u}} = \alpha_{\mathrm{v}}\frac{\mathrm{d}T}{\mathrm{d}t} - \kappa_T\frac{\mathrm{d}p_{\mathrm{e}}}{\mathrm{d}t} + \rho\sum_j \frac{v_j}{m_j}\frac{\mathrm{d}Y_j}{\mathrm{d}t} - \vec{k}_{\mathrm{u}}\cdot\frac{\mathrm{d}\vec{r}_{\mathrm{grid}}}{\mathrm{d}t} \tag{64}$$

where p_{e} is the imposed thermodynamic pressure and $\vec{r}_{\mathrm{grid}}$ is the grid vector. For implicit calculations of $\vec{u}$, numerical accuracy requires either a grid size Δr such that $|k_{\mathrm{u}}\Delta r| \ll 1$ or $\vec{u}\longrightarrow \mathrm{d}\vec{r}_{\mathrm{grid}}/\mathrm{d}t$. For a very large gradient region, this is resolved by a semi-implicit mixing of $\vec{k}_{\mathrm{u}}$ with its last step value. The quantities ρ, α_{v}, κ_T and v_j are calculated from the state equation.

The equations are discretized in a finite difference form, and to insure computational stability we use variable upwind differencing of the convection terms in regions of large gradients. The degree of upwinding is based on matching the film layer results. In the quasi-steady limit, the convection–diffusion equations feature a local spatial variation that depends exponentially on the local computational cell Pe_{grid} (this is the basis for the film layer equations). To be consistent with this limit, the difference equations three-point spatial stencil for the convective terms have weights (i.e., degree of upwinding) proportional to exponents of signed Pe_{grid}. For small Peclet numbers, this gives a central difference; for large Peclet numbers, the full upwind difference is approached. To insure computational accuracy, the r coordinate is given by a time dependent grid, and due to expected sharp gradients the grid spacing is smallest near the drop boundary. The grid motion is determined by fixing one boundary at the initial interface, and by choosing the outermost boundary, $R_{\mathrm{e}}(t)$, to follow the fluid motion (Lagrangian far field boundary); $\mathrm{d}R_{\mathrm{e}}/\mathrm{d}t = u(r = R_{\mathrm{e}})$. Relative to the local grid motion, the effective convection velocity is thus $(u - \mathrm{d}r_{\mathrm{grid}}/\mathrm{d}t)$. The boundary conditions are satisfied at the drop center (null gradients) and at the far field boundary (specified values of the dependent variables). The thermodynamic variables are calculated at grid cell centers, whereas the velocity and fluxes are calculated at grid cell boundaries (Roache, 1976).

Since $Ma \ll 1$, the pressure is calculated as $p(r,\ t) = p_e(t) + p'(r,\ t)$ where $p_e(t)$ is specified and $p'(r, t)$ is a small perturbation calculated from the momentum equation. At any time step, the solution is found by iterating in two sequential pairs. The first pair is u and p' representing the flow dynamics; the second pair is T and Y_1 representing the flow thermodynamics. An iterate of the flow dynamics pair is done in two steps: First, Eqs. (61) and (62) are used to calculate u with the very small p' being neglected. Second, Eq. (18) is used to calculate p' whose value relative to p_e is smaller than the numerical error tolerance. The second pair of variables, (T, Y_1) is obtained by iteratively solving Eqs. (19) and (20) as a pair of coupled convection–diffusion equations. The difference equations for the time dependent vectors of cell center (T, Y_1) values are thus in the form of coupled matrix equations. To satisfy the jump conditions at the drop boundary, we modify the matrix elements that are related to cells at the drop boundary according to Eqs. (35)–(40) and the film layer equations.

During any particular time step, an iterate is accomplished by a two stage process: first, there is a partial explicit time step predictor, followed by an implicit time step corrector. The convection–diffusion equations are discretized using a three-point spatial stencil. and this yields difference equations in the form of tridiagonal matrices including the T and Y_1 cross-coupling matrices. Since these cross-coupling matrices are second order in time differences, the implicit time step is calculated to first order using the Thomas algorithm for inverting tridiagonal matrices (Anderson et al., 1984), followed by iteration through matrix multiplications to obtain a second order time step. Because the time constant associated with Eq. (30) is very small, the equations are very stiff, and therefore during each time step iterate a separate iteration is necessary to calculate the boundary conditions as explained above. These conditions are then used in the radial velocity calculations and in the formation of the (T, Y_1) vector pair matrices. During each simulation, the time step is adjusted dynamically based upon the previous time step convergence.

5. Results

The present simulations are performed for an *n*-heptane drop in nitrogen because it is the set of binary substances which is best documented experimentally. The equations of state have been calculated according to the procedure described in Harstad et al. (1997) and the calculation of properties has been described in Harstad and Bellan (1998). The purpose of these simulations is first to validate the model, and then to explore parametric regimes of practical interest that are unavailable experimentally such as the small size drops typical of gas turbine combustors and Diesel engines. Since all droplet data spanning subcritical to supercritical regimes is for large drops, our first set of simulations is for these conditions. The only data that can be used for comparisons is that obtained under evaporative rather than burning conditions, since in the last case the flame temperature that acts as the far field boundary is unknown. Furthermore, as shown below, it is only microgravity data that can be considered valid for these comparisons because normal gravity data has unavoidable convective effects that are not modeled here. Additionally, since all high pressure microgravity drop evaporation experiments were performed with suspended drops, even these data are clearly not totally equivalent to our simulation results which are obtained for a free floating drop.

In all calculations presented here $\alpha_{aj} = 1$ for all j's according to the data of Paul (1962).

5.1. Model validation

To our knowledge, microgravity obtained data with C_7H_{16} drops evaporating in N_2 were reported only by Sato (1993) and Nomura et al. (1996). In their experiments 0.7–1 mm drops were suspended from a fiber of 200 μm diameter whose influence was not assessed; however, recent calculations (see Morin, 1999) indicate that the influence of the fiber increases with increasing temperature and pressure. For example, it was found that for drops of 1 mm diameter at 300 K the heat flux from the fiber may be ~7 and 10% of the heat provided by the surrounding nitrogen at 473 K and 0.1 MPa, and 673 K and 1 MPa, respectively. Also not reported by Nomura et al. (1996) is the ratio of the measured gravity by the normal gravity during the experiments as a function of time; only average microgravity ratios of 10^{-2} for parabolic flights and 10^{-3} for drop towers are cited. The transient value of the microgravity ratio might be important to ascertain when comparing numerical results and data since Vieille et al. (1996) have shown that if the magnitude of this ratio is in the range 10^{-4}–10^{-2}, buoyancy effects are still identifiable in the evaporation constant.

The C_7H_{16} drop evaporation experiments of Chauveau et al. (1993) were conducted only in normal gravity, whereas their reported microgravity experiments were of burning drops. Therefore, our comparison focuses on the data of Sato (1993) and Nomura et al. (1996) while also considering for reference (see Table 2) the more recent normal gravity data of Morin et al. (1999) for 1–1.5 mm drops, instead of that of Chauveau et al. (1993).

Table 2
Maximum regression rate of the maximum density gradient location, K in mm^2/s, obtained from the current model (ap), Nomura et al.'s (Nomura et al., 1996) microgravity experimental data (Nom), Sato's (Sato, 1993) microgravity and normal gravity experimental data (Sat), and Morin et al.'s (Morin et al., 1999) normal gravity data (Mor)[a]

p_e (MPa)	T_e (K)	K (μg)	K (normal g)	K_{ap}	K_{ap}/K_{data} (μg)
0.1	470	0.116 (Nom)	0.22 (Mor)	0.135	1.16
0.1	655	0.306 (Nom)	0.45 (Mor)	0.280	0.92
0.1	745	0.390 (Nom)	0.56 (Mor)	0.350	0.90
0.5	470	0.117 (Nom)	–	0.135	1.15
0.5	655	0.356 (Nom)	–	0.320	0.90
0.5	745	0.437 (Nom)	–	0.390	0.89
1.0	470	0.138 (Nom)	–	0.135	0.98
1.0	655	0.424 (Nom)	–	0.330	0.78
2.0	445	0.097 (Sat)	0.14 (Sat)	0.0935	0.97
2.0	452	0.096 (Nom)	–	–	–
2.0	655	0.475 (Nom)	–	0.360	0.76
2.0	745	0.4–1.7 (Nom)	0.450	–	–
5.0	495	0.2–0.13 (Nom)	–	0.140	0.70–1.08

[a] The Nomura et al.'s and Morin et al.'s data were provided by the authors, and Sato's values were read on their graph following the directions given in their paper. In the simulations $T_d^0 = 300$ K and $d^0 = 0.7$ mm, while Nomura et al.'s d^0 was 0.6–0.8 mm, Sato's was 1 mm, and Morin et al.'s was 1–1.5 mm.

The simulations were performed for nominal initial conditions (superscript 0) matching the experimental data: $R_d^0 = 0.35$ mm except for the comparison with Sato's (Sato, 1993) data which was performed for $R_d^0 = 0.5$ mm, and $T_{d,b}^0 = 300$ K. The far field conditions are located at $R_e^0 = 4$ mm where T_e and p_e are specified consistent with those of the experiments and $Y_{le}^0 = 0$. The fluid drop is initially composed of pure heptane ($T_c = 540.3$ K, $p_c = 2.76$ MPa), while the surrounding is nitrogen ($T_c = 126.2$ K, $p_c = 3.39$ MPa); in order to avoid an initial unphysical discontinuity, a minute amount of heptane exists initially in the drop surroundings, its distribution vanishing with increasing r. For the same reason, although the fluid drop temperature and outer fluid composition are assumed initially uniform, a set of computational initial conditions (i.e. spatial profiles of the variables) are calculated for each simulation by satisfying the nominal initial conditions at the domain boundaries and the boundary conditions at R_d. In practice, this is achieved by choosing target values for

$$\eta_Y \equiv \left(\frac{\mathrm{d}Y}{\mathrm{d}r}\right)_{r=R_d} \frac{R_d^0}{(1-\varepsilon_r)\left[Y_e^0 - Y^0\left(R_d^0\right)\right]} \quad \text{and} \quad \eta_T \equiv \left(\frac{\mathrm{d}T}{\mathrm{d}r}\right)_{r=R_d} \frac{R_d^0}{(1-\varepsilon_r)\left[T_e^0 - T^0\left(R_d^0\right)\right]} \tag{65}$$

where $\varepsilon_r \equiv R_d^0/R_e^0 \ll 1$, and iterate on the values of η_Y, η_T and the dependent variables at the surface ($Y_1^0(R_d^0)$, $T^0(R_d^0)$ and F_{ems}) until convergence is achieved or until a minimal deviation from the targets is obtained. For example, at $p = 0.1$ MPa we initially choose $\eta_Y = \eta_T = 1$ in anticipation of the well known (Williams, 1965) quasi-steady analytic solution, and the iteration confirms these values at convergence. Another example is that of a calculation performed at $p = 1$ MPa where although the initial choice is still $\eta_Y = \eta_T = 1$, the initial conditions iterate converges with $\eta_Y = \eta_T = 0.88$. As the initial pressure increases, η_Y and η_T depart further form unity. It is these calculated initial profiles which appear in all figures as those at $t = 0$ s, and that are used to continue the calculations for $t > 0$ s.

In all of the discussions below, 'subcritical' and 'supercritical' qualifications will be used with respect to the heptane critical point, and not with respect to the critical point of the mixture which varies according to the local composition.

5.1.1. Determination of thermal diffusion factors from high temperature data

As discussed previously, values of α_{BK} are poorly known for most substances, except at atmospheric conditions where they can be calculated from kinetic theory. Since we are here interested in calculations at considerably larger pressures, the question arises as how to calculate α_{BK}. For this purpose, the premise is that if it can be shown, for example, that α_{IK} is very small, in fact it may be considered negligible with respect to $(\alpha_{BK} - \alpha_{IK})$ in Eq. (26) and then $\alpha_{BK} \simeq -\alpha_h$ (see Eq. (48)). Since α_h is calculated from thermodynamics, this would provide an approximate value for α_{BK} at each p for all (Y_1, T) conditions where $|\alpha_{IK}/\alpha^*| \ll 1$ and $\alpha^* \equiv \max_{(Y_1,T)}|\alpha_h|$. The exact definition of α^* may vary according to the needs of the calculation; what is important is that α^* represents in average the magnitude of α_h in the thermodynamic region of interest. A similar premise may be made regarding α_{BK}. The purpose of these high temperature data comparisons is to explore whether either premise is approximately correct.

Shown in Fig. 1a are $(d/d^0)^2$ plots from our simulations portraying Nomura et al.'s (Nomura et al., 1996) experiments at high temperature (745 K) in the pressure range of 0.1–2 MPa. For consistency with optical measurements, the location of the drop boundary is defined

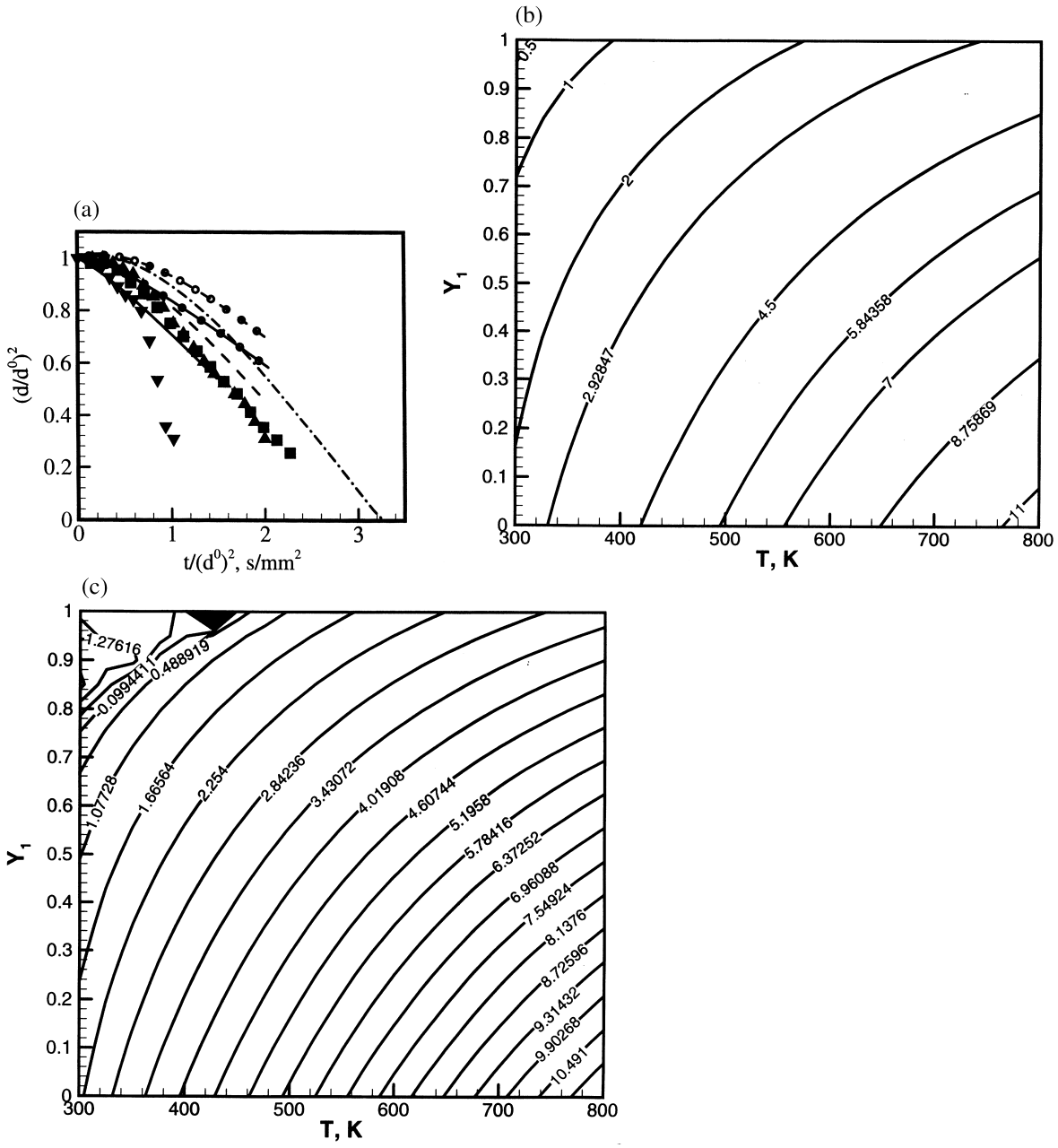

Fig. 1. (a) High temperature comparisons. $R_d^0 = 0.35$ mm; $R_e^0 = 4$ mm, $Y_e^0 = 0$ and $T_{d,b}^0 = 300$ K. In the far field T_e and p_e are specified as in the experiments. Simulations at $T_e = 745$ K and p_e: 0.1 MPa, $\alpha_{IK} = 0.01$ ——; 0.1 MPa, $\alpha_{BK} = 0.01$ —○—; 0.5 MPa, $\alpha_{IK} = 0.01$ - - - -; 0.5 MPa, $\alpha_{BK} = 0.01$ - - ○ - -; 2 MPa – · –. Data: 741 K and 0.1 MPa ■; 749 K and 0.5 MPa ▲; 746 K and 2 MPa ▼. (b) Contour plots of α_h defined in Eq. (27) for $p = 0.1$ MPa. (c) Contour plots of α_h defined in Eq. (27) for $p = 0.5$ MPa.

in the simulations as that of the maximum density gradient. In agreement with well known theory (Williams, 1965), at 0.1 MPa the liquid/gas interface is found to be precisely that of maximum density gradient. With increasing p the two locations still coincide for all simulations in the range 0.1–10 MPa investigated in this work, but the density gradient, although still substantial, decreases across the boundary as p increases.

All but two of our simulations were conducted with $\alpha_{IK} = 0.01$; the remaining simulations were conducted with $\alpha_{BK} = 0.01$. Our 0.1 MPa results with $\alpha_{IK} = 0.01$ capture the linear part of the 0.1 MPa data very well but display a somewhat earlier d^2-law behavior; it is unclear whether the non-coinciding part of the data and simulations fall within the experimental error since this error is not provided with the data. In contrast, the 0.1 MPa simulations with $\alpha_{BK} = 0.01$ capture the 0.1 MPa during the early, heating period, but departs substantially from the data in the linear regime. This behavior is initially puzzling since $\lim_{p\to 0}\alpha_{BK} = \alpha_{KT}$ and thus one would expect that the low pressure behavior will be better rendered numerically when α_{BK} is specified. Our interpretation of the results is that even at low pressure α_{BK} is not constant or small, and in fact is a function of T and Y_1 that is better approximated by $-\alpha_h$ in the spatial region of strong mass fraction and temperature gradients (i.e. near the drop boundary) where the Soret and Dufour terms may be important. If this statement is correct, then it should not be surprising that for small α_{IK} the numerical simulations agree with the data since Eq. (34) shows that $\alpha_{BK} \simeq -\alpha_h$ when $|\alpha_{IK}/\alpha^*| \ll 1$. To verify this conjecture, α_h is plotted at 0.1 MPa as a function of Y_1 and T in Fig. 1b. It is clear that for $\alpha_{IK} = 0.01$, $|\alpha_{IK}/\alpha^*| \lesssim O(10^{-2})$, therefore justifying the premise.

Similarly, comparisons between the 0.5 MPa data and results from simulations with both α_{BK} and α_{IK} specified as 0.01 show clearly that the $\alpha_{BK} = 0.01$ results fall short of agreement with the data, and in fact show a typically large increase in the evaporation time; this is typical of results obtained with $\alpha_{BK} = 0.01$ at other pressures as well (see below). In contrast, the $\alpha_{IK} = 0.01$ results capture the nonlinear portion of the curve very well with a small discrepancy in the total evaporation time. To show that the assumption $|\alpha_{IK}/\alpha^*| \ll 1$ holds for $\alpha_{IK} = 0.01$ at 0.5 MPa, α_h is displayed in Fig. 1c; simple evaluations show that $|\alpha_{IK}/\alpha_h| \lesssim O(10^{-3})$.

Simulations and data at 2 MPa (see Fig. 1a) agree only during the initial time, after which the simulations display the expected smooth variation consistent with drop heating, whereas the data exhibit two discontinuities that can be explained only by the presence of the suspending fiber. Calculated slopes of the linear part of the curves, called the evaporation constant (Williams, 1965), K, are presented in Table 2 for comparison with the 0.1 and 0.5 MPa, $\alpha_{IK} = 0.01$ results. Despite the presence of the suspending fiber in the experiments, there is excellent agreement between simulations and data. A similar comparison cannot be performed at 2 MPa since there is no evidence of linear behavior in the data.

5.1.2. Confirmation of thermal diffusion factors from intermediate temperatures data

Displayed in Fig. 2a are $p = 2$ MPa comparisons of simulation results at 655 K for various values of α_{IK}, one simulation where α_{BK} instead of α_{IK} is prescribed, and Nomura et al.'s (Nomura et al., 1996) data at 656 K. The numerical predictions are a very weak function of α_{IK} in the range -0.6 to 0.6 and agree remarkably well with the data during the initial heat up period of the drop. Eventually, the data shows a faster evaporation than our simulations, although the lack of error bars in the data make it impossible to evaluate the extent of the

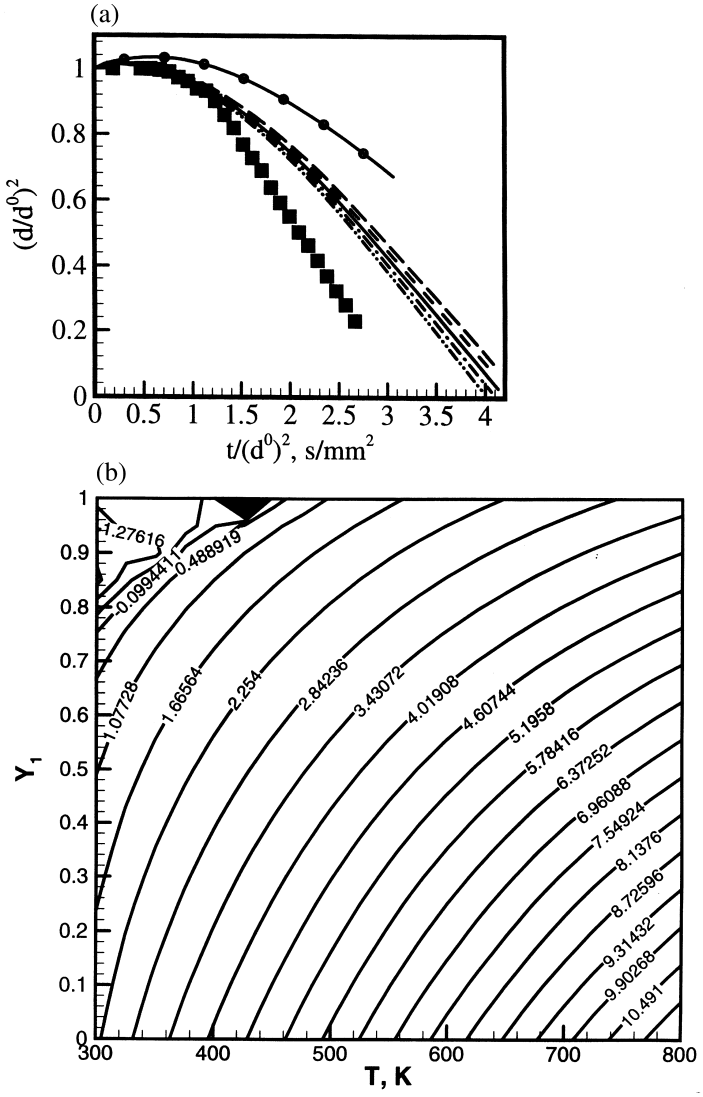

Fig. 2. (a) Intermediary temperature comparisons at 2 MPa. $R_{\mathrm{d}}^0 = 0.35$ mm; $R_{\mathrm{e}}^0 = 4$ mm, $Y_{\mathrm{e}}^0 = 0$ and $T_{\mathrm{d,\,b}}^0 = 300$ K. Simulations at 655 K; $\alpha_{\mathrm{IK}} = 0.01$ ——; 0.3 - - -; -0.3 – · – ·; -0.6 – ·· –; 0.6 — —; $\alpha_{\mathrm{BK}} = 0.01$ —●— Data at 656 K: ■. (b) Contour plots of α_h defined in Eq. (27) for $p = 2$ MPa.

disagreement. It is also difficult to evaluate the influence of the fiber (during the experiment) on the evaporation process. However, results with $\alpha_{\mathrm{BK}} = 0.01$ clearly overestimate both the growth of the drop during the initial heat up time and the drop evaporation time; these results are consistent with those of Fig. 1a. Therefore, it is apparent that at 2 MPa, the approximation $|\alpha_{\mathrm{IK}}/\alpha^*| \ll 1$ must hold as well. This conjecture is substantiated by plots of α_h displayed in Fig. 2b. In fact, contour plots of α_h at increasing pressure show that the approximation $|\alpha_{\mathrm{IK}}/\alpha^*| \ll 1$ becomes increasingly justified for $\alpha_{\mathrm{IK}} \lesssim O(10^{-1})$.

Additional comparisons between numerical predictions and data is portrayed in Fig. 3 where

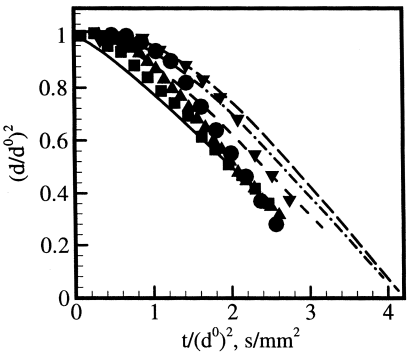

Fig. 3. Intermediary temperature comparisons. $R_d^0 = 0.35$ mm; $R_e^0 = 4$ mm, $Y_e^0 = 0$ and $T_{d,b}^0 = 300$ K. Simulations at 655 K: 0.1 MPa ——; 0.5 MPa - - - -; 1 MPa – · – ·; 2 MPa — —. Data: 648 K and 0.1 MPa ■; 655 K and 0.5 MPa ▲; 669 K and 1 MPa ▼; 656 K and 2 MPa ●.

comparisons are made in the range 0.1–2 MPa between simulations at 655 K with $\alpha_{IK} = 0.01$, and data in the range 648–669 K. The initial heating time is again very well reproduced by the simulations, except that the predictions at 0.1 MPa display again an earlier d^2-law behavior. The evaporation time is very well reproduced at 0.1 MPa, and less well as the pressure increases. Since it is difficult to quantify the influence of the suspending fiber as the pressure increases, we can qualify this comparison as very encouraging.

Table 2 includes comparisons of K for this intermediary temperature regime, and shows excellent to good agreement between data and predictions.

This study indicates that the value of α_{IK}/α^* is indeed small and that $\alpha_{BK} \simeq -\alpha_h$ is correct. The assumption made in all calculations presented below is that α_{IK} has the same small value determined at high temperatures regardless of the (p, T) conditions, and thus that $\alpha_{BK} \simeq -\alpha_h$. This assumption might not be entirely valid, as in general α_{IK} is a function of both p and T.

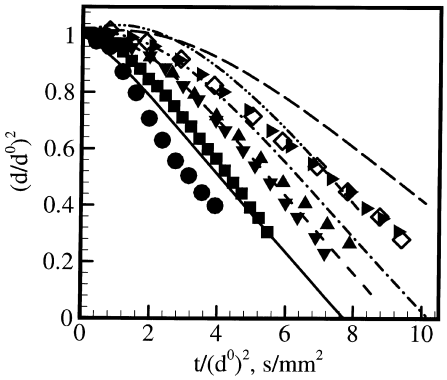

Fig. 4. Low temperature comparisons. $R_d^0 = 0.35$ mm except at 445 K where $R_d^0 = 0.5$ mm; $R_e^0 = 4$ mm, $Y_e^0 = 0$ and $T_{d,b}^0 = 300$ K. Simulations at 470 K: 0.1 MPa ——; 0.5 MPa - - -; 1 MPa –·–·; at 445 K and 2 MPa — —; at 495 K and 5 MPa –··–. Data: 471 K and 0.1 MPa ■; 468 K and 0.5 MPa ▲; 466 K and 1 MPa ▼; 445 K and 2 MPa ◇; 452 K and 2 MPa ▶; 493 K and 5 MPa ●.

This assumption and the fact that the data is from suspended drop experiments whereas our calculations are for free drops, might explain the 15–20% discrepancies (see below and Table 2) between data and results from simulations.

5.1.3. Comparison with data at low temperatures

The low temperature data of Nomura et al. (1996) and Sato (1993) (Sato's data was approximated from his figure) is shown in Fig. 4 along with our numerical predictions at 445, 470 and 495 K using $\alpha_{IK} = 0.01$. The temperature range for Nomura et al.'s (Nomura et al., 1996) data is 466–493 K whereas Sato's (Sato, 1993) data was obtained at 445 K; the data in Nomura et al. (1996) is in the 0.1–5 MPa range, whereas that of Sato (1993) is at 2 MPa. The comparisons are very good at low p and deteriorate as p increases. The predictions and data (Nomura et al., 1996) agree remarkably well at 0.1 and 0.5 MPa, whereas at 1 MPa the evaporation time is slightly overpredicted by the simulations. Nevertheless, the calculated and measured evaporation constants (Table 2) show very good agreement at all three pressures. The 2 MPa numerical results approximate the d^2 experimental variation (Sato, 1993) fairly well, and the agreement in the value of K (Table 2) is excellent. At $p = 5$ MPa, our simulation of a free drop shows an increased heating time, whereas the suspended drop in the experiment shows a decreased heating time with respect to the 0.1 MPa case. The difference between the experimental conditions and those of the simulations explains the disagreement in the heat up time, although the rate of regression of the largest gradient location is surprisingly well predicted. Since at 5 MPa the conditions may be supercritical at the drop boundary, there may be no evaporation and the concept of evaporation constant may be irrelevant, although comparisons between the rates of regression are still meaningful.

5.2. Small drops at high ambient temperatures

The above comparison between numerical predictions and data shows that the theory is capable of capturing the physics of fluid drop behavior over a substantial range of temperatures and pressures in both the subcritical and supercritical regimes. These comparisons were conducted for the relatively large drops that can be handled experimentally, although the regime of practical interest is that of smaller drops (for which experiments are not available). To address this regime of practical interest, simulations relevant to Diesel engine and gas turbine engine drop sizes and (p, T) conditions were performed with $R_d^0 = 60 \times 10^{-4}$ cm, $T_{d,b}^0 = 325$ K (the fluid drop temperature is assumed initially uniform), $R_e^0 = 0.05$ cm, $T_e^0 = 800$ K, $Y_e^0 = 0$, and p_e being either constant or specified as a function of t (see Fig. 5a). These simulations are listed in Table 3.

5.2.1. Temporal variation

5.2.1.1. Constant pressure simulations. The temporal variation of significant variables is illustrated in Fig. 5 and the lines/symbols used in the figures are those in Table 3. For these small drops, the 0.1 MPa behavior is exactly that predicted by the classical theory (Williams, 1965): Fig. 5b shows the totally linear behavior of d^2 as the drop heats up very rapidly. As p increases, the heating time occupies a larger time of the drop lifetime (defined as the time

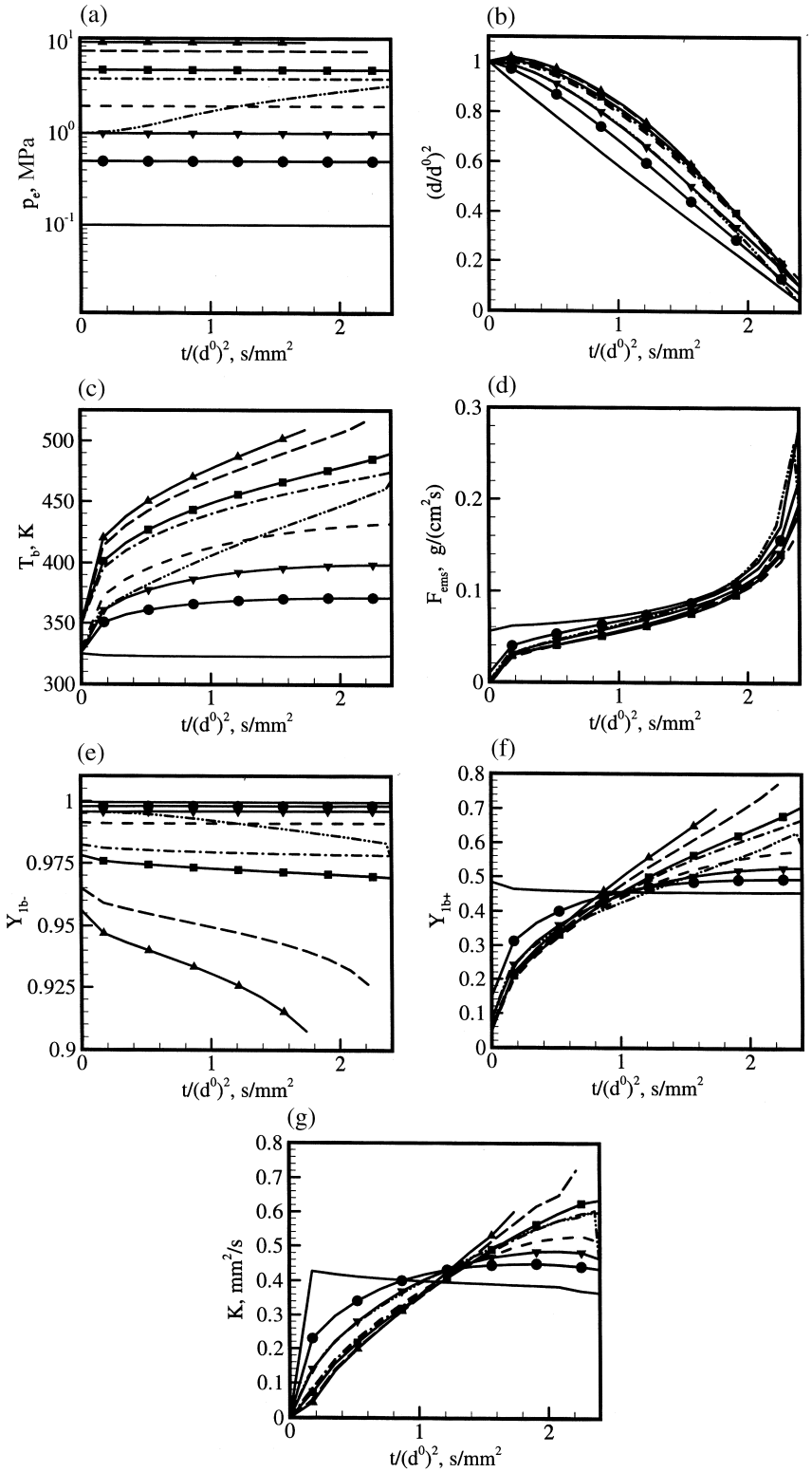

Fig. 5. Temporal variations from simulations with $R_d^0 = 6 \times 10^{-2}$ mm, $T_{d,b}^0 = 325$ K, $R_e^0 = 0.5$ mm, $T_e^0 = 800$ K, and $Y_e^0 = 0$. The legend is shown in Table 3. (a) p_e, (b) $(d/d^0)^2$, (c) T_b, (d) F_{ems}, (e) Y_{1b-}, (f) Y_{1b+}, and (g) K.

Table 3
List of simulations conducted with drops of 60 μm radius. The far field temperature was 800 K and constant, and the initial drop temperature was 325 K

p_e (MPa)	Lines/Symbols
0.1	
0.5	
1.0	
2.0	
4.0	
5.0	
8.0	
10.0	
Transient	

during which one can identify a large density gradient) and the variation of d^2 is no longer initially linear. Eventually, at large pressures the drop size (as measured by the location of the largest density gradient) initially increases before starting to decrease. At high p the linear variation is no longer obtained even after the initial heat up time.

The increasing nonmonotonicity of the temporal variation of d^2 with increasing pressure was experimentally observed by Nomura et al. (1996) and Chauveau et al. (1993) for n-heptane in air, although the last authors attributed it to the influence of the drop suspension fiber. Just as in the present simulations, Nomura et al. (1996) observed that the ratio of the heat-up time to the drop lifetime (defined there as the value of the abscissa at the intersection with the d^2 curve) increases with increasing p.

The evolution of the boundary temperature (Fig. 5c) shows a segregation into the lower temperatures achieved at subcritical conditions whose maximum is limited by the boiling point at the particular pressure, and the higher temperatures achieved at supercritical conditions whose maximum is limited only by the far field value. The emission rate displayed in Fig. 5d has a true physical meaning only for the subcritical simulations where it represents the evaporation rate. The fact that the F_{ems} values become eventually similar does not invalidate the previous statement that $F_{ems} \ll \rho D_{eff}/\Delta r^-$ at supercritical conditions and that $F_{ems} \gg \rho D_{eff}/\Delta r^-$ at strong evaporative subcritical conditions; what changes substantially as one transitions from one regime to another is the value of $\rho D_{eff}/\Delta r^-$, not F_{ems}. The very large values of F_{ems} towards the end of each simulation are an artifact of the small drop size.

Figs. 5e and f illustrate the heptane mass fractions in the drop side of the boundary and on the pure nitrogen side of the boundary, respectively. At 0.1 MPa the drop composition remains pure heptane throughout the drop lifetime. As the pressure increases, solubility effects become increasingly important and nitrogen penetrates the fluid drop, thus explaining the decreasing value of the heptane mass fraction on the inner part of the drop boundary, $Y_{1b-} \equiv Y_1(R_d^-)$. At low pressures, Y_{1b-} attains an asymptotic behavior that is not seen for $p > 8$ MPa. The 0.1 MPa behavior displayed by the heptane mass fraction on the outer part of the drop boundary, $Y_{1b+} \equiv Y_1(R_d^+)$, is that of the classical (Williams, 1965) quasi-steady behavior at atmospheric p:

after a very short and slight nonuniformity Y_{1b+} remains constant throughout the drop lifetime. As p increases but remains subcritical, the initial unsteadiness relaxes to an approximately asymptotic state. In contrast, as p further increases and the supercritical regime is reached, even after the relaxation of the initial transient, Y_{1b+} continues to increase without reaching an asymptote. These results show that laminar diffusional mixing at supercritical conditions is more effective than quiescent evaporation at all subcritical pressures (see explanation below).

To explore the variation of K with p, its variation is presented in Fig. 5g. It is clear from the plots that it is only at 0.1 MPa that K can be considered to be truly a constant (after the short initial transient behavior). In the remaining cases, the transients persist during an important part of the drop lifetime. Even at subcritical pressures, with increasing pressure the asymptotic behavior becomes increasingly problematic. At supercritical pressures, K becomes the rate of regression of the maximum density gradient boundary, and persists to increase with time.

5.2.1.2. Transient pressure simulation. The results for a transient pressure simulation are presented also in Fig. 5 for comparison with the constant pressure simulations. The imposed pressure on the drop yields initially subcritical conditions (0.5 MPa) and eventually supercritical conditions (4 MPa). Such calculations crossing the critical point are problematic if the focus is on the transcritical behavior because the critical point is a thermodynamic singularity: C_p becomes infinite; α_D, the latent heat and the surface tension become null; etc. It is well known that one of the important characteristics of the critical point is that correlation lengths become very large and the integral conservation equations may not be necessarily convertible to a differential form; this implies that the Navier–Stokes equations may not be valid in the critical/transcritical regime. However, if the emphasis of a calculation is not necessarily on the critical/transcritical behavior, one may still use this formalism and refrain from giving too much credence to the results around the thermodynamic singularity. It should be additionally realized that calculations encompassing the critical point will always be numerically difficult, and that their convergence will be sensitive to the initial conditions. Since we did not make any special provisions for the initial conditions of this simulation, the fact that the calculation was successfully performed can be attributed to the robustness of the model.

Given these warnings, our results show that the drop displays a behavior intermediate between the sub- and supercritical one, and that Y_{1b+} (Fig. 5f) is somewhat reduced with respect to that of the drop which was constantly exposed at the highest pressure of the transient simulation.

5.2.2. Spatial variation at different pressures

5.2.2.1. Comparisons of sub- versus supercritical variation. The spatial variations of T, ρ, Y, the compression factor $Z = pv/(R_u T)$, α_D, the traditional Lewis number $Le = \lambda/(nC_p D)$ and Le_{eff} are presented in Fig. 6(a)–(g) for the 0.1 MPa simulation and equivalent results are shown in Fig. 7(a)–(g) for the 5 MPa case.

As discussed above, one of the major differences between sub- and supercritical behavior is evidenced by the drop temperature variation which is negligible at 0.1 MPa, being limited by the boiling point at that pressure; in contrast the drop temperature continuously increases at 5

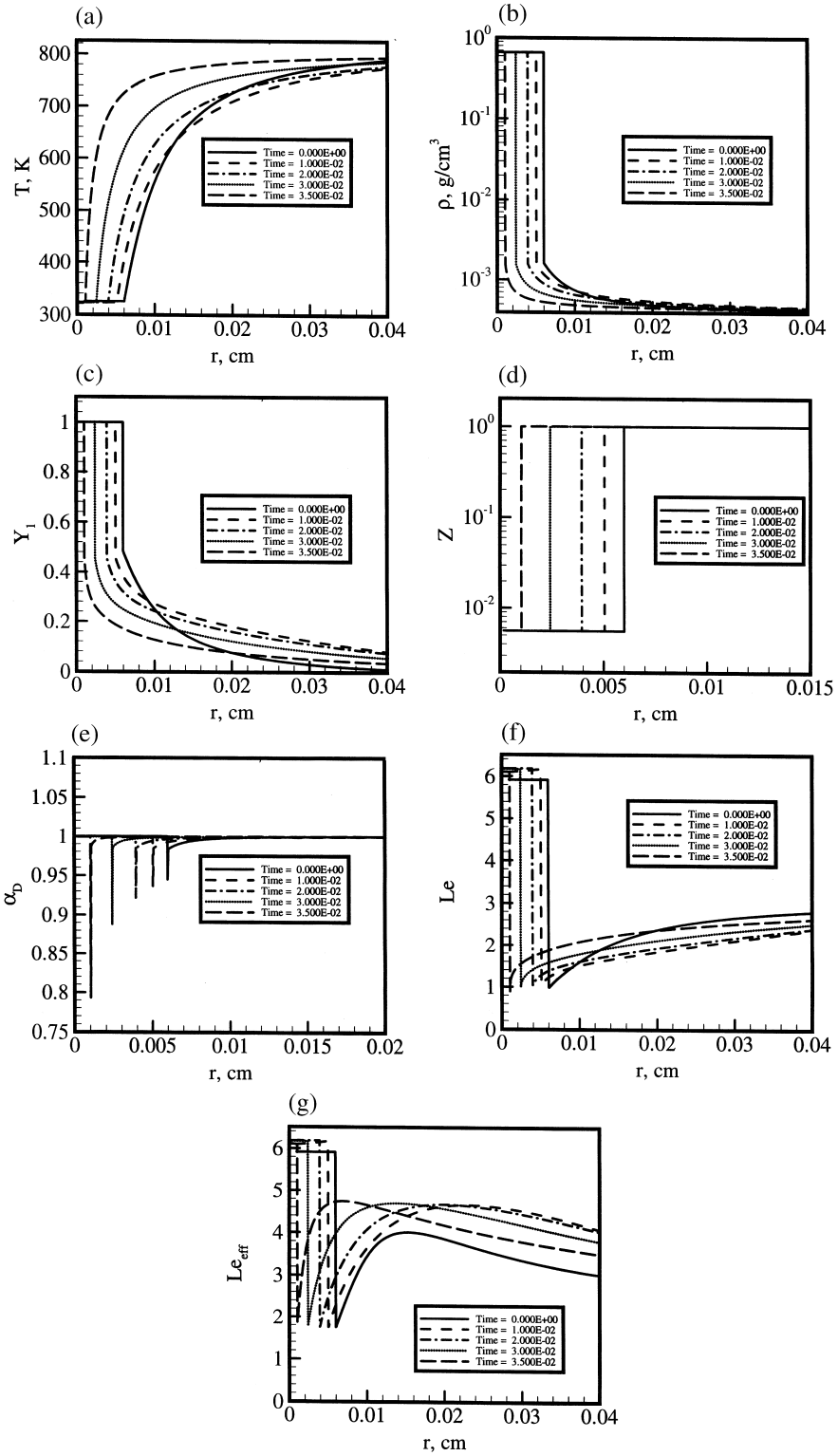

Fig. 6. Spatial variations of (a) T, (b) ρ, (c) Y, (d) Z, (e) α_D, (f) Le, and (g) Le_{eff} for $R_{\text{d}}^0 = 6 \times 10^{-2}$ mm, $T_{\text{d, b}}^0 = 325$ K, $R_{\text{e}}^0 = 0.5$ mm, $T_{\text{e}}^0 = 800$ K, $Y_{\text{e}}^0 = 0$ and $p_{\text{e}} = 0.1$ MPa. Legend for t is in s.

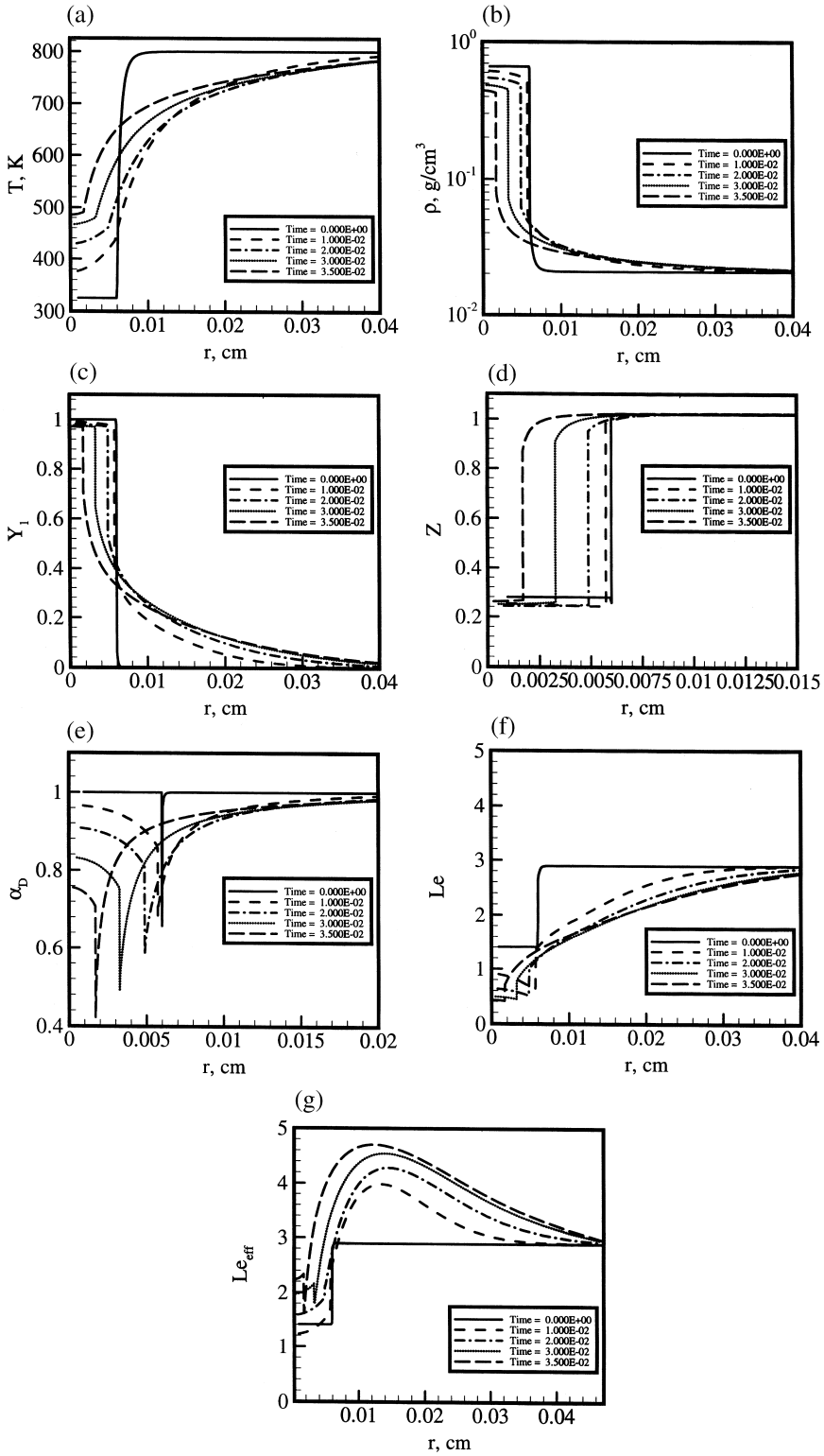

Fig. 7. Spatial variations of (a) T, (b) ρ, (c) Y_1, (d) Z, (e) α_D, (f) Le, and (g) Le_{eff} for $R_{\text{d}}^0 = 6 \times 10^{-2}$ mm, $T_{\text{d,b}}^0 = 325$ K, $R_{\text{e}}^0 = 0.5$ mm, $T_{\text{e}}^0 = 800$ K, $Y_{\text{e}}^0 = 0$ and $p_{\text{e}} = 5$ MPa. Legend for t is in s.

MPa. While the heptane mass fraction remains unity within the drop at 0.1 MPa and the drop surface regresses, a small amount of nitrogen dissolves into the drop at 5 MPa and the internal drop heptane mass fraction is reduced from its initial value of 1. Moreover, while at any given location in the vicinity of the drop original boundary the heptane mass fraction decreases with time at 0.1 MPa, it increases with time at 5 MPa. This opposite trend is the result of the difference between the vigorous evaporation which continuously enlarges the drop sphere of influence, and thus dilutes the amount of heptane, and the slow supercritical diffusion process which slightly contracts temporarily the sphere of influence before an asymptotic recovery of its original value. This change in R_e is also affecting the density which is substantially larger outside of the drop at 5 MPa.

The compression factor, Z, and mass diffusion factor, α_D, are thermodynamic quantities that characterize departures from the perfect gas behavior and from ideal mixtures, respectively; for a perfect gas $Z = 1$ and for an ideal mixture $\alpha_D = 1$. As expected, at 0.1 MPa the compression factor is unity in the gas, and $O(10^{-3})$ in the drop which is a value characterizing liquids. In contrast, at 5 MPa the compression factor decreases from the unity value outside of the drop to $\sim$0.25 inside the drop showing that the drop is no longer a liquid despite its liquid-like density. At 0.1 MPa, the mass diffusion factor is unity everywhere except at and very close to the drop surface where there is a mixture of heptane and nitrogen. In contrast, at 5 MPa there are departures from the unity value in the entire field, and these departures increase with time as nitrogen continues to dissolve in the drop and the mass fraction of heptane increases in the initially pure nitrogen region (as discussed above).

The variations of Le and Le_{eff} are displayed in Figs. 6f and g for the 0.1 MPa simulations and Figs. 7f and g for the 0.5 MPa predictions. At 0.1 MPa, Le and Le_{eff} are identical inside the drop showing that indeed Le_{eff} reaches the correct limit for a single substance, a uniform temperature, and atmospheric conditions. However, even at atmospheric conditions one observes differences from 50% to a factor of 2–3 between Le and Le_{eff} in regions where there is a mixture of substances and there are temperature gradients. At 5 MPa these differences increase even further: Le and Le_{eff} are initially identical, but Le decreases whereas Le_{eff} increases with time from the initial condition. Mistakenly, the Le values inside the drop are typical of an ideal gas ($Le \leq 1$), whereas Le_{eff} correctly indicates the existence of a dense gas ($Le_{\mathrm{eff}} > 1$). The incorrect (correct) Le (Le_{eff}) predictions have both a fundamental and a practical significance, in that engineering estimates of combustor dimensions are often based upon calculations of nondimensional numbers such as the Lewis number. The present simulations show that classical evaluations of the Lewis number may give erroneous results.

5.2.2.2. Spatial profiles comparisons. Presented in Fig. 8(a)–(d) are spatial variations of T, Y_1, ρ, and α_D at 3×10^{-2} s, for 0.1, 2, 4, 8 MPa and the transient run; results obtained at 10 MPa are not illustrated because of their similarity with those at 8 MPa. The selected time is such that the leftover drop mass is small, and the choice of the pressures is such that the atmospheric pressure is retained as a reference, the critical point is 'framed' by two pressures, the pressure is increased by a constant ratio, and the entire range is relevant to both gas turbine and Diesel engines. Parallel plots are presented in Fig. 9(a)–(d) at the output time which is clo-

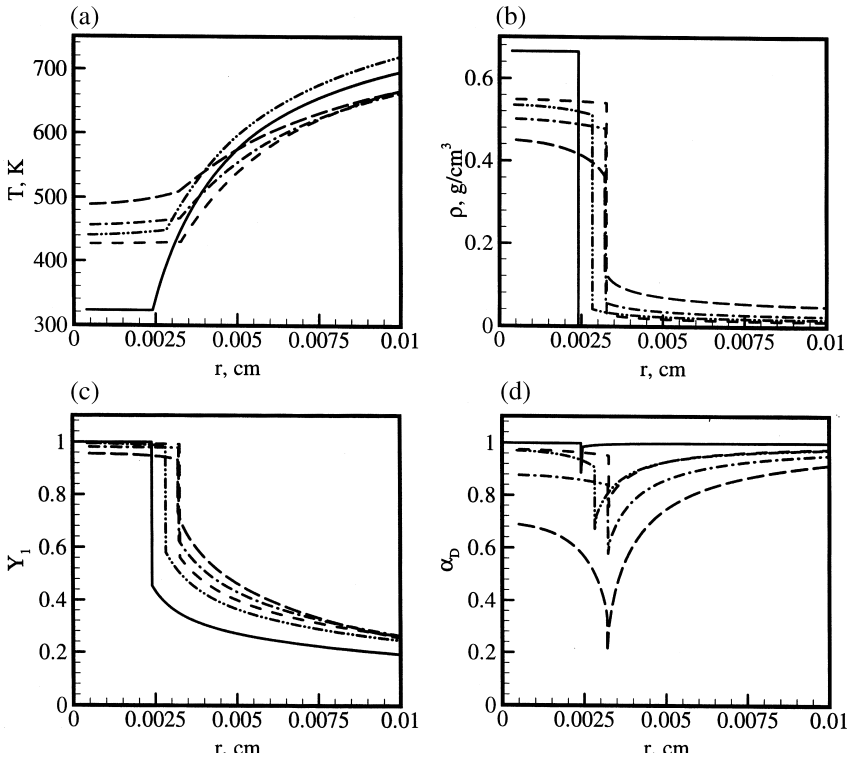

Fig. 8. Spatial variations at 3×10^{-2} s of (a) T, (b) ρ, (c) Y_1 and (d) α_D for $R_d^0 = 6 \times 10^{-2}$ mm, $T_{d,b}^0 = 325$ K, $R_e^0 = 0.5$ mm, $T_e^0 = 800$ K, $Y_e^0 = 0$ and $p_e = 0.1$ MPa ——, 2 MPa - - - -, 4 MPa – · – ·, 8 MPa — —, MPa and transient – ·· –.

sest to the half-mass time (for the selected times, the maximum error with respect to the exact half-mass is 2%) to explore the possibility of profile similarity at the same stage in the drop lifetime. Clearly, such a similarity does not exist and it can be concluded that it is not only the time scales that change as the pressure increases from subcritical to supercritical, but it is the general behavior of the drop that is different.

Although the half mass time is approximately the same for most illustrated simulations (for 0.1, 2, 4, 8 MPa and the transient case it occurs at respectively 1.25×10^{-2}, 1.75×10^{-2}, 1.75×10^{-2}, 1.75×10^{-2} and 1.6×10^{-2} s), at a fixed time close to the drop disappearance the maximum gradient region is variable whereas at the half mass time it is more similar. We conclude that pressure specific differentiation in size occurs when the drop becomes relatively small, and therefore data must be obtained close to the time of drop disappearance in order to identify distinctive pressure dependent behavior. In contrast to ρ which is more distinctive as a function of p at larger times, T displays a pressure specific behavior at all times; therefore, a temperature measurement will always be a good relative pressure indicator. The magnitude variation of α_D, which is a good indicator of (diffusion/convective) mixing, displays much more differentiation close to the drop disappearance than at the half mass time, and the low values

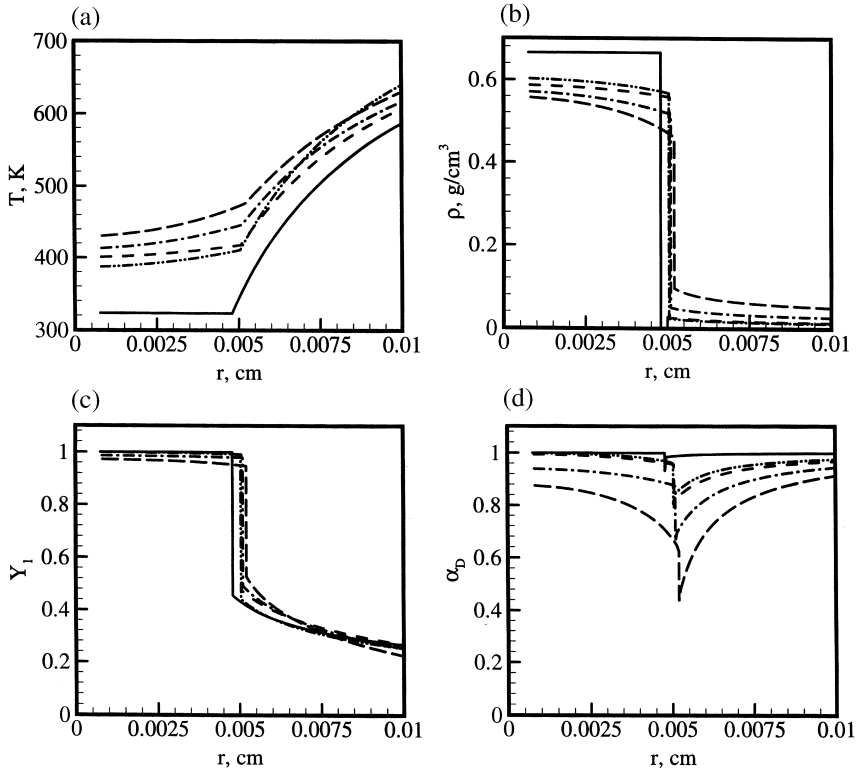

Fig. 9. Half-mass spatial variations of (a) T, (b) ρ, (c) Y_1 and (d) α_D for $R_d^0 = 6 \times 10^{-2}$ mm, $T_{d,b}^0 = 325$ K, $R_e^0 = 0.5$ mm, $T_e^0 = 800$ K, $Y_e^0 = 0$ and $p_e = 0.1$ MPa ——, 2 MPa - - - -, 4 MPa – · – ·, 8 MPa — —, MPa and transient – ·· –.

attained at 8 MPa show that the drop might be close to its critical point for the particular composition at that location.

6. Conclusions

A model of fluid behavior under both sub- and supercritical thermodynamic conditions has been discussed with particular emphasis on the different physics according to the initial conditions with respect to the drop substance critical point. The model has been exercised for a fluid drop for which data are available for model validation. Initially the drop is colder than its surroundings whose far field conditions are prescribed. In the subcritical regime and for large emission rates from the drop, there exists a film layer in the inner part of the drop surface and the solution of the equations has a convective–diffusive character. In the supercritical regime, there is no material surface to follow, and this introduces an indeterminacy in the boundary conditions. To resolve this indeterminacy one must follow an arbitrary boundary of interest which is chosen here to be that of the initial fluid drop. The solution has then a pure diffusive

character, and from this solution we calculate the location of the highest density gradient which we identify with the optically observable fluid drop.

Experimental validation of the model requires that substance properties be accurately specified, and we therefore analyzed the definitions of different transport properties. Our analysis shows that both the Irwing–Kirkwood and the Bearman–Kirkwood defined transport parameters may differ from the measurable values, and we define transport parameters that correctly converge to the kinetic theory values in the low pressure limit.

The model was exercised for a heptane drop in nitrogen because of the existing data available for comparison. Simulations obtained with this model were validated with microgravity experimental data for large drops over a wide range of temperatures and pressures. The large temperature data were used to determine the value of the thermal diffusion factor and further validations were conducted with this fixed value. The agreement between predictions and d^2 data is excellent at atmospheric pressure and becomes fair at supercritical pressure, whereas the rate of regression of the point of maximum density gradient is remarkably well predicted at all pressures. Discrepancies between numerical results and data are attributed to both the influence of the suspending fiber in the experiments which affects heat transfer, and to the insufficient level of microgravity which affects buoyancy, as well as to uncertainties in the values of the thermal diffusion factor. The numerical predictions show that the traditional d^2-law is obeyed only in the subcritical regime. As the pressure is increased, d^2 becomes nonmonotonic with time, with a slope whose magnitude increases as a function of time. Thus, we initially identify a heating period during which the drop size may increase, followed by a period during which the size is continuously reduced. The duration of the heat-up period increases with far field pressure.

Numerical predictions were also made for the small drops of practical interest for which data is not available. In the simulations, the heptane drops were initially at 325 K whereas the surrounding nitrogen was at 800 K. Results were obtained from simulations at constant far field pressure in the range 0.1–10 MPa, and for a far field transient pressure crossing the critical point. Comparisons between subcritical and supercritical simulations show that the drop temperature increases only slightly at atmospheric conditions and remains constant thereafter (being constrained by the boiling point), whereas it continuously increases at supercritical conditions. This, and the difference between vigorous evaporation coupled to strong convection at atmospheric conditions and slow diffusion at supercritical conditions explains the larger heptane mass fraction near the drop boundary at supercritical conditions. Despite the liquid like density, the fluid drop under supercritical conditions has properties similar to those of a dense gas. It is shown that the classically calculated Lewis number cannot differentiate between liquid and dense gas, but an effective Lewis number previously derived correctly predicts the characteristics of supercritical behavior. Results obtained from simulations with a transient far field pressure crossing the heptane critical point show that the drop combines characteristics of both subcritical and supercritical behavior. It is also indicated that transcritical results should be interpreted with caution since due to the very large correlation lengths, it is doubtful that the Navier–Stokes equations hold in that regime.

Acknowledgements

This research was conducted at the Jet Propulsion Laboratory under sponsorship from the National Aeronautics and Space Administration, the Lewis Research Center with Dr. Daniel L. Bulzan as technical contract monitor. His continuing interest and support are greatly appreciated. We also want to thank Prof. Hiroshi Nomura of Nihon University in Chiba, Japan, and Prof. Iskender Gökalp of the Centre National de la Recherche Scientifique in Orléans, France, for providing us with their data.

References

American Petroleum Institute, 1992. Technical Data Book — Petroleum Refining, 5th ed.

Anderson, D.A., Tannehill, J.C., Pletcher, R.H., 1984. Computational Fluid Mechanics and Heat Transfer. Hemisphere, NY.

Bert, J., Dupuy-Philon, J., 1997. Microgravity measurement of the Soret effect in a molten salts mixture. J. Phys.: Condens. Matter 9, 11045–11060.

Bird, R.B., Stewart, W.E., Lightfoot, E.N., 1960. Transport Phenomena. Wiley, New York.

Bou-Ali, M.M., Ecenarro, O., Madariaga, J.A., Santamaria, C.M., Valencia, J.J., 1998. Thermogravitational measurements of the Soret coefficient of liquid mixtures. J. Phys.: Condens. Matter 10, 3321–3331.

Chapman, S., Cowling, T.G., 1970. The mathematical theory on nonuniform gases. Cambridge University Press, Cambridge.

Chauveau, C., Chesnau, X., Gökalp, I., 1993. Burning characteristics of *n*-heptane droplets AIAA 93-0824. In: 31st Aerospace Sciences Meeting, Reno, NV.

Delplanque, J-P., Sirignano, W.A., 1993. Numerical study of the transient vaporization of an oxygen droplet at sub- and super-critical conditions. Int. J. Heat Mass Transfer 36 (2), 303–314.

Ecenarro, O., Madariaga, J.A., Navarro, J., Santamaria, C.M., Carrion, J.A., Saviron, J.M., 1990. Fickian and thermal diffusion coefficients from liquid thermogravitational columns. J. Phys.: Condens. Matter 2, 2289–2296.

Ecenarro, O., Madariaga, J.A., Navarro, J., Santamaria, C.M., Carrion, J.A., Saviron, J.M., 1993. Thermogravitational separation and the thermal diffusion factor near critical points in binary liquid mixtures. J. Phys.: Condens. Matter 5, 2289–2294.

Givler, S.D., Abraham, J., 1996. Supercritical droplet vaporization and combustion studies Prog. Energy Combust. Sci 22, 1–28.

Haldenwang, P., Nicoli, C., Daou, J., 1996. High pressure vaporization of LOX droplet crossing the critical condition. Int. J. Heat Mass Transfer 39 (16), 3453–3464.

Harstad, K., Bellan, J., 1998. Isolated fluid oxygen drop behavior in fluid hydrogen at rocket chamber pressures. Int. J. Heat Mass Transfer 41, 3537–3550.

Harstad, K., Bellan, J., 1999. The Lewis number under supercritical conditions. Int. J. Heat Mass Transfer 42, 961–970.

Harstad, K.G., Miller, R.S., Bellan, J., 1997. Efficient high pressure state equations. A.I.Ch.E. J 43 (6), 1605–1610.

Hirshfelder, J.O., Curtis, C.F., Bird, R.B., 1964. Molecular Theory of Gases and Liquids. Wiley, New York.

Keizer, J., 1987. Statistical Thermodynamics of Nonequilibrium Processes. Springler–Verlag, New York.

Law, C.K., Law, H.K., 1982. A d^2-law for multicomponent droplet vaporization and combustion. AIAA Journal 20 (4), 522–527.

Li, W.B., Segrè, P.N., Sengers, J.V., Gammon, R.W., 1994. Non-equilibrium fluctuations in liquids and liquid mixtures subjected to a stationary temperature gradient. J. Phys.: Condens. Matter 6, A119–A124.

Morin, C., 1999. Studies on the influence of pressure and temperature on the vaporization of hydrocarbon droplets. Ph.D. Thesis. Centre National de la Recherche Scientifique, Orléans, France.

Morin, C., Chauveau, C., Gökalp, I., 1999. Studies on the influence of pressure and temperature on the vaporization of *n*-heptane droplets. In: ILASS-Europe Conference.

Nomura, H., Ujiie, Y., Rath, H.J., Sato, J., Kono, M., 1996. Experimental study on high pressure droplet evaporation using microgravity conditions. In: 26th Symp. (Int.) on Comb, 1267–1273.

Paul, B., 1962. Compilation of evaporation coefficients. ARS J 32, 1321–1328.

Prausnitz, J., Lichtenthaler, R., de Azevedo, E., 1986. Molecular Thermodynamics for Fluid-Phase Equilibrium. Prentice-Hall, Englewood Cliffs, NJ.

Reid, R.C., Prausnitz, J.M., Polling, B.E., 1987. The Properties of Gases and Liquids, 4th ed. McGraw-Hill, New York.

Roache, P.J., 1976. Computational Fluid Dynamics. Hermosa Publishers, Albuquerque, NM.

Sarman, S., Evans, D.J., 1992. Heat flux and mass diffusion in binary Lennard-Jones mixtures. Phys Rev A45 (4), 2370–2379.

Sato, J., 1993. Studies on droplet evaporation and combustion in high pressures AIAA 93-0813. In: 31st Aerospace Sciences Meeting, Jan. 11–14, Reno, NV.

Singh, K., Dham, A.K., Gupta, S.C., 1983. Symmetric diffusion and thermal diffusion ratios for a ternary gas mixture. J. Phys. B: At. Mol. Phys 16, 2613–2618.

Vieille, B., Chauveau, C., Chesnau, X., Odeïde, A., Gökalp, I., 1996. High-pressure droplet burning experiments in microgravity. In: 26th Symp. (Int). on Combustion, 1259–1265.

Vogelsang, R., Hoheisel, J., 1988. The Dufour and Soret coefficients of isotopic mixtures from equilibrium molecular-dynamics calculations. J. Chem. Phys 89, 1588–1591.

Williams, F.A., 1965. Combustion Theory. Addison-Wesley, Reading, MA.

Yang, V., Lin, N., Shuen, J-S., 1994. Vaporization of liquid oxygen (LOX) droplets in supercritical hydrogen environments. Combust. Sci. and Tech 97, 247–270.